Cell Reports

Article

# Targeting the GPI transamidase subunit GPAA1 abrogates the CD24 immune checkpoint in ovarian cancer

## Graphical abstract

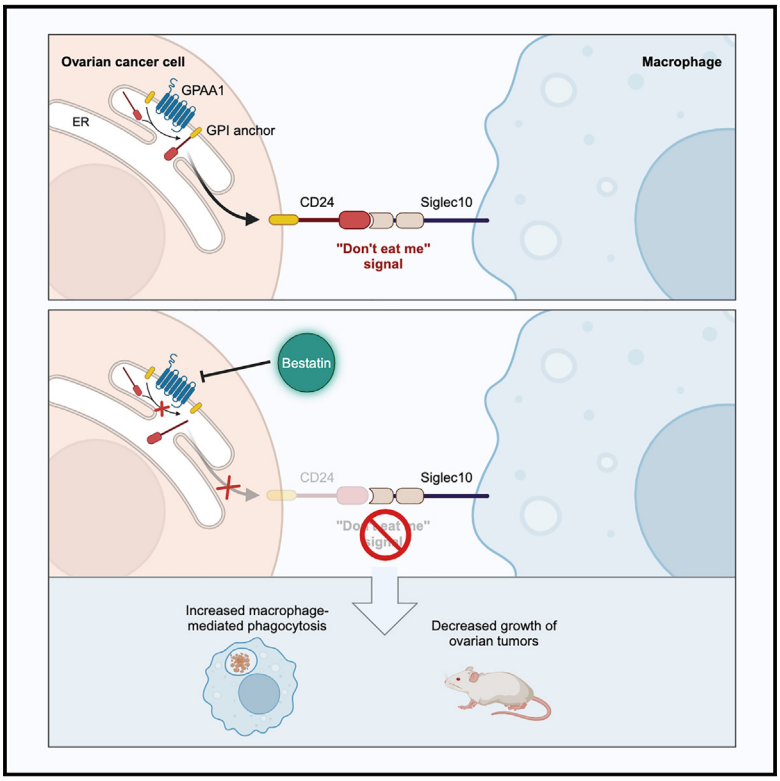


## Highlights

- GPAA1 promotes cell surface expression of the anti-phagocytic signal CD24
- GPAA1 knockout enhances macrophage-mediated phagocytosis of ovarian cancer cells
- GPAA1 knockout suppresses growth of ovarian tumors in mice xenografts
- Bestatin, an aminopeptidase inhibitor, inhibits GPAA1 and suppresses tumor growth

## Authors

Alok K. Mishra, Tianyi Ye, Shahid Banday, ..., Frank Eisenhaber, Sunil K. Malonia, Michael R. Green

## Correspondence

alok.mishra@umassmed.edu (A.K.M.), frank@eisenhaber.org (F.E.), sunil.malonia@umassmed.edu (S.K.M.)

## In brief

Mishra et al. identify the GPI transamidase complex subunit GPAA1 as a factor required for cell surface expression of CD24 and show that genetic or pharmacological inhibition of GPAA1 enhances macrophage-mediated phagocytosis and suppresses ovarian tumor growth in mice. Their results highlight a potential immunotherapeutic approach for CD24$^{+}$ ovarian cancers.

Mishra et al., 2024, Cell Reports *43*, 114041
April 23, 2024 
https://doi.org/10.1016/j.celrep.2024.114041

CellPress

Cell Reports

CellPress
OPEN ACCESS

Article

# Targeting the GPI transamidase subunit GPAA1 abrogates the CD24 immune checkpoint in ovarian cancer

Alok K. Mishra,[1,*] Tianyi Ye,[1] Shahid Banday,[1] Ritesh P. Thakare,[1] Chinh Tran-To Su,[2] Ngoc N.H. Pham,[3] Amjad Ali,[1] Ankur Kulshreshtha,[1] Shreya Roy Chowdhury,[1] Tessa M. Simone,[1] Kai Hu,[1] Lihua Julie Zhu,[1,4] Birgit Eisenhaber,[2,5] Sara K. Deibler,[1] Karl Simin,[1] Paul R. Thompson,[6] Michelle A. Kelliher,[1] Frank Eisenhaber,[2,5,7,*] Sunil K. Malonia,[1,8,*] and Michael R. Green[1]

[1]Department of Molecular, Cell and Cancer Biology, University of Massachusetts Chan Medical School, Worcester, MA 01605, USA
[2]Bioinformatics Institute (BII), Agency for Science, Technology, and Research (A*STAR), 30 Biopolis Street, Matrix, #07-01, Singapore 138671, Singapore
[3]Faculty of Biology and Biotechnology, University of Science, Vietnam National University, 227 Nguyen Van Cu Street, District 5, Ho Chi Minh City, Vietnam
[4]Program in Molecular Medicine and Department of Genomics and Computational Biology, University of Massachusetts Chan Medical School, Worcester, MA 01605, USA
[5]Lausitz Advanced Scientific Applications (LASA) gGmbH, Straße der Einheit 2–24, 02943 Weißwasser, Germany
[6]Department of Biochemistry and Molecular Biotechnology, University of Massachusetts Chan Medical School, Worcester, MA 01605, USA
[7]School of Biological Sciences, Nanyang Technological University (NTU), 60 Nanyang Drive, Singapore 637551, Singapore
[8]Lead contact
*Correspondence: alok.mishra@umassmed.edu (A.K.M.), frank@eisenhaber.org (F.E.), sunil.malonia@umassmed.edu (S.K.M.)
https://doi.org/10.1016/j.celrep.2024.114041

## SUMMARY

CD24 is frequently overexpressed in ovarian cancer and promotes immune evasion by interacting with its receptor Siglec10, present on tumor-associated macrophages, providing a "don't eat me" signal that prevents targeting and phagocytosis by macrophages. Factors promoting CD24 expression could represent novel immunotherapeutic targets for ovarian cancer. Here, using a genome-wide CRISPR knockout screen, we identify GPAA1 (glycosylphosphatidylinositol anchor attachment 1), a factor that catalyzes the attachment of a glycosylphosphatidylinositol (GPI) lipid anchor to substrate proteins, as a positive regulator of CD24 cell surface expression. Genetic ablation of GPAA1 abolishes CD24 cell surface expression, enhances macrophage-mediated phagocytosis, and inhibits ovarian tumor growth in mice. GPAA1 shares structural similarities with aminopeptidases. Consequently, we show that bestatin, a clinically advanced aminopeptidase inhibitor, binds to GPAA1 and blocks GPI attachment, resulting in reduced CD24 cell surface expression, increased macrophage-mediated phagocytosis, and suppressed growth of ovarian tumors. Our study highlights the potential of targeting GPAA1 as an immunotherapeutic approach for CD24$^{+}$ ovarian cancers.

## INTRODUCTION

Ovarian cancer is the second most common gynecologic cancer and the leading cause of gynecologic malignancy-related deaths in the United States.[1] The standard treatment for newly diagnosed ovarian cancer includes cytoreductive (debulking) surgery followed by chemotherapy.[2] However, recurrence affects 25% of early-stage patients and 70%–80% of advanced-stage patients,[3,4] highlighting the urgent need to explore alternative therapeutic strategies.

Immuno-oncology strategies have demonstrated remarkable success in stimulating immune responses against diverse tumor types and have significantly improved patient outcomes. For example, conventional immune checkpoint inhibitors targeting the PDL1/PD1 pathway have shown efficacious responses in several solid cancers, such as malignant melanoma, non-small-cell lung cancer, and urothelial cancer.[5] However, in ovarian cancers, PDL1/PD1 inhibitors have shown limited efficacy.[6–8]

Recent studies have identified the CD24-Siglec10 immune checkpoint as a promising therapeutic target in ovarian cancer.[9] CD24 is a highly glycosylated cell adhesion protein that is linked to the plasma membrane by a glycosylphosphatidylinositol (GPI) anchor.[9] CD24 is primarily expressed by immune cells but is often highly expressed in many cancers, most notably ovarian cancer.[10,11] CD24 facilitates immune evasion by interacting with Siglec10, a transmembrane protein present on the surface of tumor-associated macrophages (TAMs) and providing an anti-phagocytosis ("don't eat me") signal that hinders TAMs from targeting and engulfing tumor cells.[10] Previous studies have shown that CRISPR-mediated knockout of CD24 or its blockade with an anti-CD24 monoclonal antibody enhances

TAM-mediated phagocytosis of ovarian cancer cells and inhibits tumor growth in mouse models.[10,12]

In this study, we aimed to identify factors and pathways that could be pharmacologically inhibited to reduce CD24 expression and its function; such factors could represent novel immunotherapeutic targets for ovarian cancer. As a first step, we performed a genome-wide CRISPR-Cas9 screen to identify factors that promote CD24 cell surface expression. Using this approach, we identified GPAA1 (GPI anchor attachment 1), a critical component of a multisubunit complex that facilitates attachment of a GPI anchor to substrate proteins, thereby directing them to the cell-surface membrane.[13] Interestingly, GPAA1 shares structural similarities with a specific class of aminopeptidases,[14] and we found that an aminopeptidase inhibitor, bestatin, binds to GPAA1, inhibiting its function. Genetic or pharmacological inhibition of GPAA1 in ovarian cancer cells decreased CD24 cell surface expression, increased phagocytosis by TAMs, and reduced ovarian tumor growth in mice xenografts. Our findings open a new avenue for developing small-molecule immunotherapeutics for $CD24^+$ ovarian cancers.

## RESULTS

### A genome-scale CRISPR-Cas9 knockout screen identifies factors that promote CD24 cell-surface expression in ovarian cancer

To identify factors and pathways regulating CD24 cell-surface expression in ovarian cancer, we performed a genome-wide CRISPR-Cas9 screen. To select an appropriate cell line for the screen, we performed CD24 flow cytometry analysis in a panel of human ovarian cancer cell lines. Our analysis revealed robust CD24 cell surface expression among seven of eight ovarian cancer cell lines tested (A1847, IGROV1, NCI/ADR-RES, OVCAR3, OVCAR4, OVCAR8, and SKOV3), all of which exhibited greater than ~85% $CD24^+$ cells (Figure S1A). The exception was the A2780 cell line, which was $CD24^-$. We selected the OVCAR8 cell line for the screen because it had the highest percentage of $CD24^+$ cells and is a well-characterized, high-grade serous ovarian cancer (HGSOC) cell line.[15] To ensure the suitability of OVCAR8 cells for the CRISPR-Cas9 knockout screen, we confirmed that the proliferation of OVCAR8 cells was unaffected by the loss of CD24 (Figures S1B and S1C).

For the screen, we established an OVCAR8 cell line that stably expressed active Cas9 (Figures S1D and S1E). These cells were transduced with the human Brunello CRISPR knockout pooled library, which consists of ~76,000 single guide RNAs (sgRNAs) targeting ~19,000 genes (4 sgRNAs per gene).[16] After 15 days of puromycin selection, cells were stained with an anti-CD24 antibody, and those with substantially reduced cell-surface expression of CD24 ($CD24^{low}$ cells) were isolated by fluorescence-activated cell sorting (FACS). We identified sgRNAs that were significantly enriched in the $CD24^{low}$ population relative to the unsorted population by bioinformatic analysis of deep sequencing data (Figure 1A).

Our screen yielded candidate genes representing a broad range of functional categories, including intracellular signaling, transcriptional regulation, mRNA stability, post-translational modification, and membrane trafficking (Figure 1B). As anticipated, all four sgRNAs targeting CD24 exhibited statistically significant enrichment (Figure 1B). Notably, the most highly enriched candidate in the screen was GPAA1 (Figures 1B and 1C), a component of the multisubunit GPI transamidase (GPIT) complex that mediates attachment of a GPI anchor to substrate proteins, which serves as a mechanism for directing GPI-associated proteins (GPI-APs) to the cell membrane.[17] Proteins that are destined to become GPI anchored harbor an N-terminal endoplasmic reticulum (ER) localization sequence and a C-terminal GPI attachment signal peptide and are translocated to the ER, where the attachment of a pre-synthesized GPI lipid anchor occurs.[13,18] Once the GPI anchor is attached, the protein is shuttled to the Golgi apparatus, where it undergoes fatty acid remodeling before being transported to the outer leaflet of the cell membrane. The attachment of GPI to substrate proteins is crucial for their proper localization and function.[17] In addition to GPAA1, the primary screen identified other components of the GPIT complex, including PIGK, PIGT, and PIGU (phosphatidylinositol glycan anchor biosynthesis class K, T, and U, respectively),[19] as well as other proteins involved in GPI anchor biosynthesis, including PIGM, PIGN, PIGO, and PIGP[13,20] (Figure 1B). Gene Ontology enrichment analysis of the significant hits underscored GPI anchor biosynthesis and metabolism as the most significant biological processes (Figure 1D).

We selected *GPAA1* and nine additional genes representing various functional categories for validation. We knocked down each gene using two independent short hairpin RNAs (shRNAs) and monitored CD24 cell-surface expression by flow cytometry. As shown in Figure 1E, stable knockdown of each of the 10 candidates significantly reduced CD24 cell-surface expression compared with a control non-silencing (NS) shRNA (Figures S1F and S1G). To determine whether knockdown of these candidates reduced CD24 expression at the transcriptional or post-transcriptional level, we assessed *CD24* mRNA levels by RT-qPCR. Knockdown of three of the 10 candidates (MAP3K5, SSB, and ZNF248) significantly reduced *CD24* mRNA levels, suggesting that they promote *CD24* expression at the transcriptional level (Figures 1F and S1H). Conversely, knockdown of the other seven candidates (GPAA1, PIGP, PIGT, DHRSX, C1GALT1, RAB8A, and SORL1) did not alter *CD24* mRNA levels, suggesting their potential roles in either post-transcriptional or post-translational regulation of CD24.

### GPAA1 promotes CD24-mediated inhibition of cellular phagocytosis

We focused our further investigation on GPAA1 for several reasons. First, as mentioned above, GPAA1 emerged as the top-scoring factor from the primary screen (Figures 1B and 1C). Second, previous studies have shown that GPAA1 is overexpressed in several types of cancers, including ovarian cancer.[21–24] Third, an examination of the cBio Cancer Genomics Portal[25] revealed that *GPAA1* is amplified in approximately 30% of ovarian cancers (Figure S2A). In addition, analysis of publicly available single-cell RNA sequencing (scRNA-seq) data from ovarian tumors indicated high expression of *GPAA1* in the ovarian epithelial cancer cell cluster compared with other cell types in the tumor microenvironment (Figure 2A). Interestingly, *GPAA1* was found to be co-expressed with *CD24* in the ovarian cancer cell cluster

CellPress
OPEN ACCESS

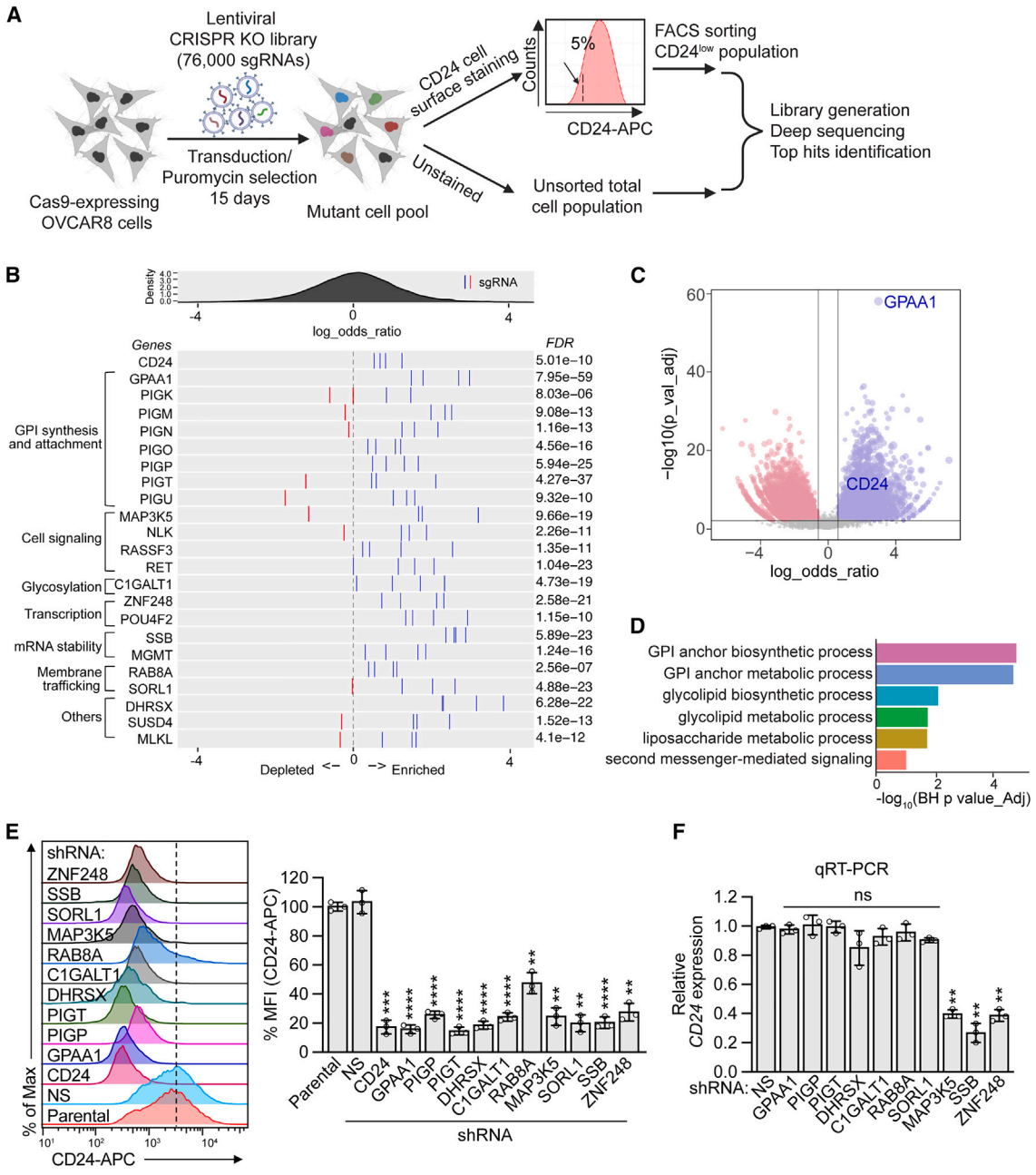


**Figure 1. A genome-scale CRISPR-Cas9 screen identifies factors that promote cell-surface expression of CD24 in ovarian cancer**

(A) Schematic of the pooled CRISPR-Cas9 screen, created with BioRender.

(B) False discovery rate (FDR) plot showing the distribution of sgRNAs targeting selected genes enriched (blue lines) or depleted (red lines) in the CD24$^{low}$ population.

(C) Volcano plot displaying significantly enriched (blue dots) or depleted (red dots) candidate genes identified from the screen. The top candidates, GPAA1 and CD24, are shown.

(D) Gene Ontology (GO) analysis showing the most significant biological processes related to the enriched sgRNAs in the CD24$^{low}$ population.

(E) Left: representative flow cytometry histograms of CD24 cell-surface expression in OVCAR8 cells expressing an shRNA targeting each candidate factor or as a control a non-silencing (NS) shRNA. Right: quantification of mean fluorescence intensity (MFI). The results were normalized to that obtained in parental OVCAR8 cells. Data are represented as mean ± SD ($n$ = 3 independent experiments).

(F) RT-qPCR analysis monitoring *CD24* expression in OVCAR8 cells expressing an NS shRNA or shRNA targeting each candidate factor. The results were normalized to that obtained with an NS shRNA. Data are represented as mean ± SD ($n$ = 3 independent experiments).

The $p$ values were calculated using one-way ANOVA followed by Dunnett's multiple-comparisons test. $^{**}p < 0.01$, $^{***}p < 0.001$, $^{****}p < 0.0001$; ns, non-significant. See also Figure S1.

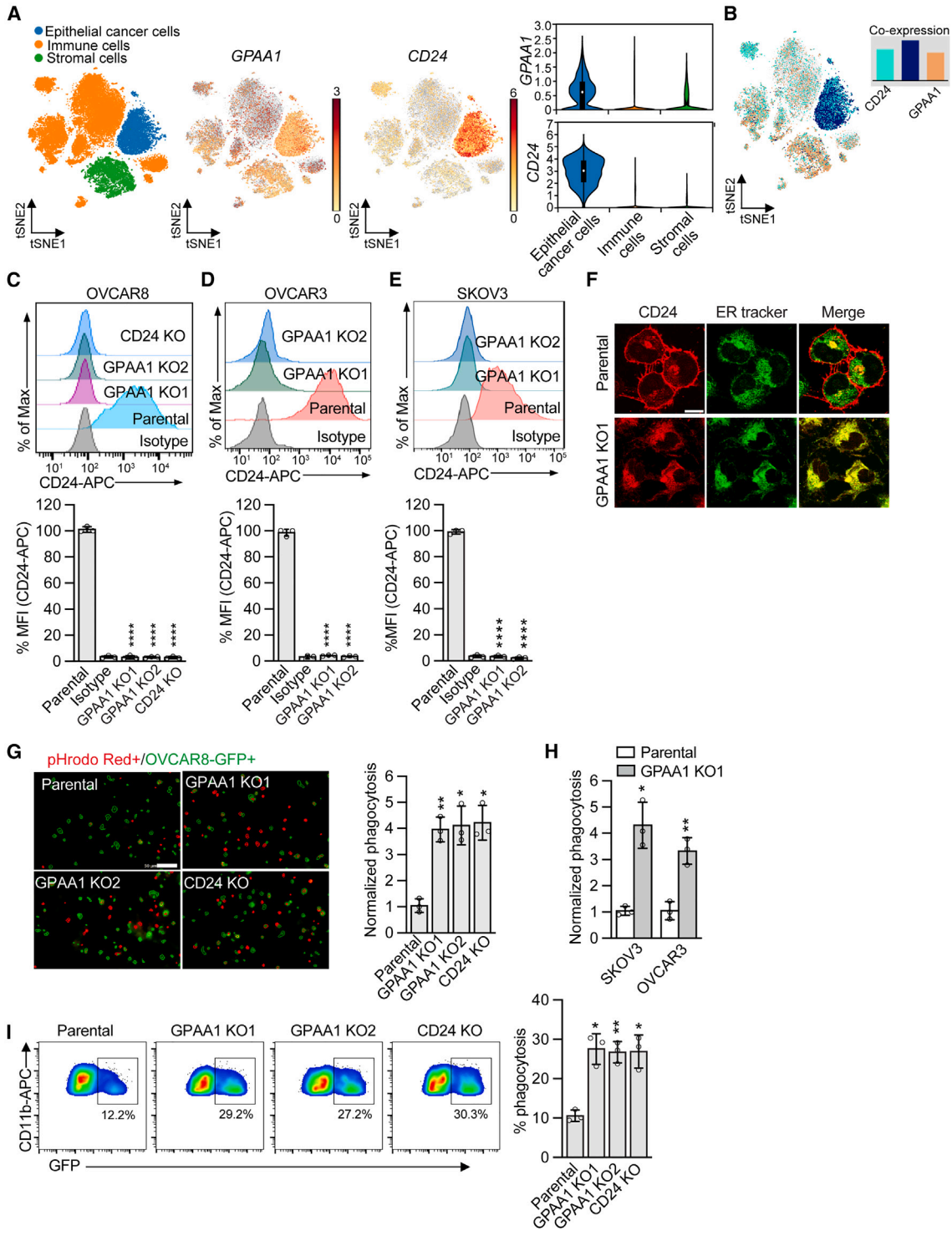


**Figure 2. GPAA1 inhibition promotes ovarian cancer cell phagocytosis**

(A) t-distributed stochastic neighbor embedding (t-SNE) and violin plots generated from a scRNA-seq dataset (GEO: GSE165897) showing expression of *GPAA1* and *CD24* in different cell types in HGSOC patient samples.

(B) t-SNE plot of scRNA-seq data showing co-expression of *GPAA1* and *CD24* in HGSOC patient samples.

(C–E) Top: representative flow cytometry histograms of CD24 cell-surface expression in parental cells and two independently derived single-cell GPAA1 KO clones (KO1 and KO2) in OVCAR8 (C), OVCAR3 (D), and SKOV3 (E) cells and in a CD24 KO OVCAR8 clone. Bottom: quantification of MFI. Data are represented as mean ± SD ($n$ = 3 independent experiments).

*(legend continued on next page)*

(Figure 2B). Furthermore, Kaplan-Meier survival analysis of publicly available gene expression datasets of patients with HGSOC[26] indicated that high expression of *GPAA1* correlates with a reduced probability of overall survival (Figure S2B). Finally, as elaborated below, GPAA1 possesses a domain with a primary sequence and predicted structure similar to metallo-aminopeptidases,[14,27] suggesting that it could potentially be inhibited by small-molecule aminopeptidase inhibitors, several of which are in advanced stages of clinical development.[28] Collectively, these observations strongly suggest that GPAA1 represents a targetable component of the GPI synthesis pathway and that its inhibition could represent an immunotherapeutic approach for ovarian cancer.

To delve deeper into the role of GPAA1 in regulating CD24 localization, we employed CRISPR-Cas9-mediated genome editing to generate two independent GPAA1 knockout clones (GPAA1 KO1 and KO2) in OVCAR8, OVCAR3, and SKOV3 cell lines (Figures S2C–S2E). As a control, we also generated a CD24 KO OVCAR8 cell line (Figure S2C). Notably, GPAA1 KO in ovarian cancer cells did not affect cell viability or proliferation (Figures S2F and S2G). As anticipated, GPAA1 KO in ovarian cancer cells completely abrogated CD24 cell-surface expression (Figures 2C–2E), without affecting *CD24* mRNA levels (Figure S2H). GPAA1 KO also abrogated cell-surface expression of other GPI-APs tested (Figure S2I) but not non-GPI-linked proteins (Figure S2J). The loss of CD24 cell-surface expression in GPAA1 KO OVCAR8 cells was also confirmed by immunocytochemistry, which revealed an accompanying accumulation of CD24 in the ER (Figure 2F). However, protein accumulation in the ER due to GPAA1 KO did not perturb the viability or proliferation of cancer cells (Figures S2F and S2G).

As mentioned previously, CD24 protects cancer cells from phagocytosis by Siglec10-expressing TAMs.[10,29,30] We hypothesized that the loss of CD24 cell surface expression observed in GPAA1 KO ovarian cancer cells would abrogate binding by Siglec10 and enhance macrophage-mediated phagocytosis. We next conducted *in vitro* phagocytosis assays following established protocols.[10,31,32] Parental, GPAA1 KO, or CD24 KO OVCAR8 cells stably expressing green fluorescent protein (GFP) were labeled with a pH-sensitive fluorescent dye (pHrodo) and co-cultured with macrophages that were derived from human peripheral blood mononuclear cells stimulated with the M2-polarizing cytokines interleukin-4 (IL-4) and IL-13 to induce Siglec10 expression[10] (Figure S2K). The total number of phagocytic events (pHrodo$^+$ cells) per well was quantified by imaging cytometry. The analysis revealed that GPAA1 KO significantly enhanced phagocytosis of OVCAR8 cells (Figure 2G). Similar results were observed with GPAA1 KO OVCAR3 and SKOV3 cells (Figure 2H). We confirmed these results using an alternative phagocytosis assay, in which phagocytic events were determined by flow cytometry to identify cells that were double-positive for GFP and the macrophage marker CD11b, indicative of macrophage-engulfed cancer cells (Figures 2I and S2L). To determine whether increased phagocytosis of GPAA1 KO cells is CD24 dependent, we expressed a GPAA1 sgRNA in A2780 cells (Figure S2M), in which CD24 expression is absent. Notably, GPAA1 KO A2780 cells were viable and did not show any proliferation defect (Figure S2N). In contrast to our results in other CD24$^+$ ovarian cancer cells, GPAA1 deficiency in A2780 cells did not enhance macrophage-mediated phagocytosis (Figure S2O), suggesting that phagocytosis occurs through a CD24-dependent mechanism. Collectively, these results indicate that genetic depletion of GPAA1 not only abrogates CD24 cell-surface expression but also enhances macrophage-mediated phagocytosis of ovarian cancer cells.

## GPAA1 KO suppresses the growth of ovarian tumors and increases survival in mice

Previous studies have shown that genetic depletion of CD24 or disruption of the CD24-Siglec10 axis enhances *in vivo* phagocytosis and suppresses tumor growth in mice.[10,30,33] Based on our results with the *in vitro* phagocytosis assays, we hypothesized that GPAA1 KO ovarian cancer cells would be susceptible to TAM-mediated phagocytosis *in vivo*, which could potentially inhibit tumor growth. To test this idea, we intraperitoneally implanted parental, GPAA1 KO, or CD24 KO OVCAR8 cells expressing GFP and luciferase into female non-obese diabetic (NOD) severe combined immunodeficiency (SCID) gamma (NSG) mice and monitored *in vivo* phagocytosis,[10] tumor growth, and survival (Figure 3A). To assess *in vivo* phagocytosis, 3 weeks post implantation, peritoneal fluid was harvested and analyzed by flow cytometry to identify cells that were double-positive for GFP and the murine macrophage marker F4/80 (Figure S3A), indicative of macrophage-engulfed OVCAR8 cells. Our results revealed that GPAA1 KO OVCAR8 tumors exhibited increased levels of *in vivo* phagocytosis by infiltrating TAMs, comparable with those observed in mice implanted with CD24 KO cells (Figure 3B). Consistent with previous findings showing a pro-inflammatory polarization of macrophages following loss of CD24,[10] we observed a higher occurrence of pro-inflammatory M1-like macrophages (CD80$^+$) and reduced frequency of M2-like macrophages (CD206$^+$) in the peritoneal fluid of mice implanted with GPAA1 KO OVCAR8 cells compared with those implanted with parental OVCAR8 cells (Figures S3B and S3C).

(F) Representative confocal microscopy images of parental OVCAR8 or GPAA1 KO1 cells stained with an anti-CD24 antibody or ER tracker. Merged images are shown. Scale bar, 10 μm.

(G) *In vitro* phagocytosis assay. Left: representative microscopy images of pHrodo Red$^+$ GFP$^+$ parental, GPAA1 KO, and CD24 KO OVCAR8 cells. Scale bar, 50 μm. Right: plot showing phagocytic events (pHrodo Red$^+$ GFP$^+$ cells), which were normalized to that obtained in parental OVCAR8 cells. Data are represented as mean ± SD ($n$ = 3 independent experiments).

(H) Plot showing normalized phagocytic events (pHrodo Red$^+$ GFP$^+$ cells) in parental and GPAA1 KO SKOV3 and OVCAR3 cells. Data are represented as mean ± SD ($n$ = 3 independent experiments).

(I) Left: representative flow cytometry plots depicting the macrophage-mediated phagocytosis of parental, GPAA1 KO, and CD24 KO OVCAR8 cells. Right: quantification of phagocytic events showing double-positive macrophages (GFP$^+$ and CD11b$^+$). Data are represented as mean ± SD ($n$ = 3 independent experiments).

The $p$ values were calculated using one-way ANOVA followed by Dunnett's multiple-comparisons test. *$p$ < 0.05, **$p$ < 0.01, ****$p$ < 0.0001. See also Figure S2.

Tumor growth was monitored weekly by *in vivo* bioluminescence imaging after 1 week of implantation. We observed a significant decrease in the growth of tumors derived from GPAA1 KO OVCAR8 cells compared with those derived from parental OVCAR8 cells (Figure 3C). This reduction in tumor growth was comparable with that observed upon implantation with CD24 KO cells (Figure 3C). Additionally, mice harboring tumors derived from GPAA1 KO cells had significantly increased survival relative to mice bearing tumors derived from parental OVCAR8 cells (Figure 3D). Consistent with a previous study showing that the reduction in the growth of CD24-deficient tumors was TAM dependent,[10] we also observed that the ability of GPAA1 KO cells to form tumors was abrogated by TAM depletion (Figures S3D and S3E), confirming that the decreased tumor growth of GPAA1 KO cells was TAM dependent.

To further extend our results in an immunocompetent setting, we utilized a genetically defined syngeneic ovarian cancer mouse model. In this model, murine fallopian tube epithelial cells bearing genetic alterations typical of HGSOC are implanted into syngeneic immunocompetent mice.[34] Specifically, we used the cell line BPPNM (*Brca1*$^{-/-}$*Trp53*$^{-/-}$*R172HPten*$^{-/-}$*Nf1*$^{-/-}$*Myc*$^{OE}$)[34] and generated a Gpaa1 KO derivative using CRISPR-mediated genome editing (Figure S3F). As expected, we found that CD24 cell-surface expression was undetectable in Gpaa1 KO BPPNM cells (Figure S3G). Furthermore, akin to our findings in human ovarian cancer cell lines, Gpaa1 KO BPPNM cells exhibited enhanced macrophage-mediated phagocytosis *in vitro* (Figure S3H). Next, we intraperitoneally implanted parental or Gpaa1 KO BPPNM cells, which stably expressed luciferase and GFP, into female C57BL/6 mice, and after 3 weeks of engraftment, we performed an *in vivo* phagocytosis assay. The results demonstrated that Gpaa1 KO BPPNM cells exhibited elevated levels of *in vivo* phagocytosis by infiltrating TAMs compared with parental BPPNM cells (Figures 3E and S3I). In addition, we observed a substantial reduction in the growth of tumors derived from Gpaa1 KO BPPNM cells compared with those derived from parental BPPNM cells (Figures 3F, 3G, and S3J). Consistent with our observations in NSG mice, C57BL/6 mice bearing tumors derived from Gpaa1 KO BPPNM cells demonstrated significantly improved survival compared with mice bearing tumors derived from parental BPPNM cells (Figure 3H). Collectively, these findings indicate that the genetic ablation of GPAA1 is sufficient to enhance *in vivo* phagocytosis and impede tumor growth in xenografted mice.

Previous studies have shown that targeting phagocytic checkpoints can stimulate a robust antitumor T cell response through priming of T cells by macrophages.[35] Interestingly, correlation analysis using the Tumor Immune Estimation Resource (TIMER)[36] showed that *CD24* and *GPAA1* expression was negatively correlated with CD8$^+$ T cell infiltration in ovarian cancer (Figure S3K). To examine T cell infiltration in Gpaa1 KO tumors, we performed flow cytometry analysis of peritoneal fluid and immunohistochemistry in omental tumors. The analysis revealed a significant increase in total CD3$^+$ T cells and cytotoxic CD8$^+$ T cells within Gpaa1 KO tumors compared with tumors derived from parental BPPNM cells (Figures 3I and 3J). The elevated infiltration of CD3$^+$ T cells and CD8$^+$ T cells within Gpaa1 KO tumors underscores the subsequent activation of the adaptive immune response following enhanced phagocytosis.

## The metallo-aminopeptidase inhibitor bestatin binds to GPAA1 and impairs GPI anchoring

GPAA1 adopts a structural fold similar to that of proteins belonging to the metallo-aminopeptidase family,[14,27] which carry one or more co-catalytic metal ions (most often Zn). We therefore hypothesized that the function of GPAA1 in GPI lipid anchoring could be inhibited by small-molecule aminopeptidase inhibitors (APIs).

To test this possibility, we assessed several small-molecule APIs, including actinonin,[37] amastatin,[38] acebilustat,[39] ARM-1,[39] bestatin,[40] DG051,[41] firibastat,[42] HFI-142,[43] SC-57461A,[44] and tosedostat (CHR-2797),[45] for their ability to inhibit GPAA1 function and, consequently, reduce CD24 cell-surface expression. Flow cytometry analysis in OVCAR8 cells following treatment with these APIs revealed that actinonin, ARM-1, bestatin, HFI-142, and tosedostat significantly decreased CD24 cell-surface expression (Figure S4A). Notably, actinonin, ARM-1, bestatin, and tosedostat share similar pharmacophores, such as hydrophobic and/or aromatic groups and hydrogen bond acceptors (Figure S4B), indicating an interaction mechanism similar to their potential binding partners/receptors. As expected, none of these APIs altered the cell-surface expression of the non-GPI-linked protein HLA-A2 (a component of MHC1), except tosedostat, which showed a slight increase in HLA-A2 cell-surface expression (Figure S4C).

We selected bestatin (also known as ubenimex) for further analysis due to its well-documented potency in inhibiting multiple metallo-aminopeptidases.[40] Additionally, bestatin is a natural compound derived from *Streptomyces oliverticuli* and is known to be orally active, safe, and well tolerated.[46,47] We employed computational methods to explore the potential binding of bestatin and other APIs to GPAA1. A thorough analysis of known 3D structures of aminopeptidase-inhibitor complexes revealed that the compounds that we found to inhibit GPAA1 interact with the aminopeptidase active site via the metal ion(s), most likely Zn, located there (Figures S5 and S6A–S6C; Tables S1 and S2). In this dominant arrangement, two hydrogen acceptor functional groups from the inhibitor compound encircle the metal ion. Notably, one Zn ion is the preferred interaction partner for the inhibitor molecule, even in aminopeptidases with two metal ions in the active site (Figure 4A). The molecular mechanics and dynamics calculation results, including blind molecular docking attempts without prior knowledge of the bestatin-binding regions using AutoDock Vina,[48] show that the binding mode of bestatin and similar inhibitor compounds observed in aminopeptidase-inhibitor complex structures is the most plausible, from the energetic/binding energy point of view, for our published GPAA1 structural models, which include GPAA1$^{Zn}$ (with one Zn ion in the active site) and GPAA1$^{ZnZn}$ (with two Zn ions).[14] We also find that all observed, clinically relevant mutations of GPAA1 (except for L291P) energetically destabilize GPAA1, further supporting an active functional role for GPAA1 in the genesis of GPI-APs (Figure S6D and S6E).

In Figure 4A, the bestatin-binding pocket involving the GPAA1 Zn-binding residues D153 and D188[27] is illustrated for both the GPAA1$^{Zn}$ and GPAA1$^{ZnZn}$ models. This site was found to be the most frequently visited by the bestatin molecule in docking simulations. The bestatin molecule directly contacted the

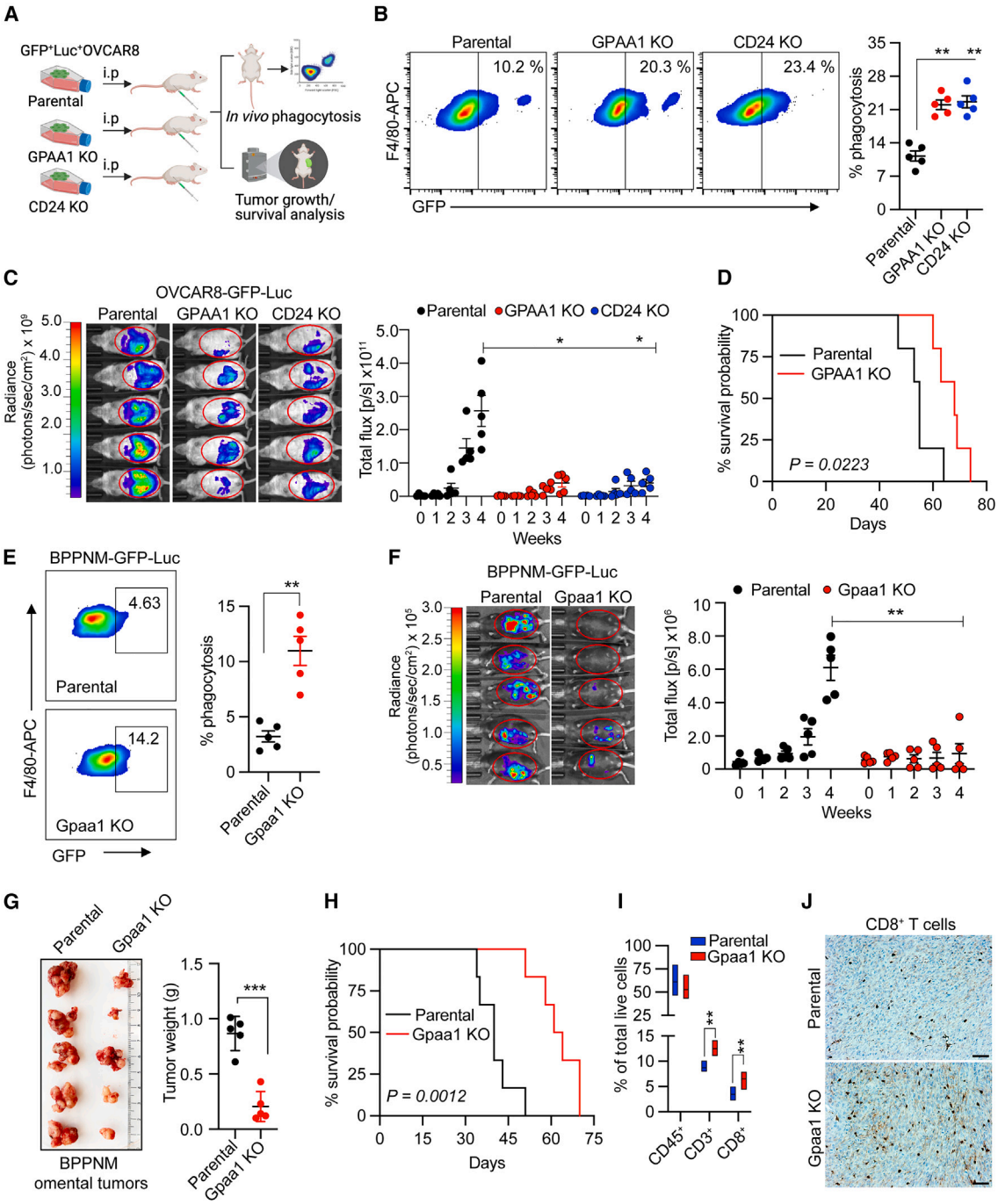


**Figure 3. GPAA1 KO suppresses the growth of ovarian tumors and increases survival in mice**

(A) Schematic outline of the experimental approach to monitor *in vivo* phagocytosis and tumor growth in mice, created with BioRender.

(B) *In vivo* phagocytosis assay. Left: representative flow cytometry plots showing phagocytotic events (GFP$^+$ F4/80$^+$ cells) of parental, GPAA1 KO, or CD24 KO OVCAR8 tumor cells; the percentage indicates the frequency of phagocytotic events of all TAMs. Right: Quantification of phagocytic events of all TAMs. Data are represented as mean ± SEM ($n$ = 5 mice per group).

(C) Left: representative *in vivo* bioluminescence images of NSG mice 5 weeks following implantation with parental, GPAA1 KO, or CD24 KO OVCAR8 cells. Right: quantification of tumor growth as measured by total flux. Data are represented as mean ± SEM ($n$ = 5 mice per group).

(D) Survival analysis of NSG mice ($n$ = 5 per group), harboring tumors derived from implantation with parental or GPAA1 KO OVCAR8 cells.

(E) Left: representative flow cytometry plots showing phagocytic events (GFP$^+$ F4/80$^+$ cells) of parental or Gpaa1 KO BPPNM tumor cells 3 weeks after implantation; the number indicates the frequency of phagocytosis events of all TAMs. Right: quantification of phagocytotic events of all TAMs. Data are represented as mean ± SEM ($n$ = 5 mice per group).

*(legend continued on next page)*

Zn(s) located in the GPAA1 active site of both $GPAA1^{Zn}$ and $GPAA1^{ZnZn}$, with a binding energy Δg (in kcal/mol) of $-5.7 \pm 1.04$ and $-5.14 \pm 0.07$, respectively. The same principal arrangement of a hydrogen bond acceptor pair from bestatin interacting with a Zn ion was also found in known 3D complexes, such as PDB: 3MDJ (one Zn) or PDB: 5IB9 (two Zn).

To confirm the physical interaction of bestatin with GPAA1, we utilized a cellular thermal stability shift assay (CETSA), a method for accessing drug-target interactions in cells.[49] OVCAR8 cells were treated with bestatin and then subjected to increasing temperatures to denature and precipitate proteins. Subsequently, cells were lysed, and the soluble protein fractions were analyzed by immunoblotting to quantify the changes in thermal stability. As shown in Figure 4B, the thermal stability of GPAA1 increased in the presence of bestatin compared with DMSO, suggesting that bestatin binds to GPAA1.

Specific biochemical assays for measuring the enzymatic activity of GPAA1 and components of the GPIT complex are not yet well established. Consequently, the functional characterization of GPIT components and the identification of factors that modulate GPIT activity have largely relied on the utilization of GPI-linked protein reporter assays.[50] We therefore utilized this reporter assay to assess the impact of bestatin treatment on GPIT activity. For this assay, we stably expressed a GPI-anchored mCherry reporter protein (fused to a streptavidin-binding peptide [SBP] tag, with an ER localization sequence at the N terminus and a GPI attachment signal at the C terminus; Figure 4C, top) in OVCAR8 cells and monitored mCherry localization by immunocytochemistry. As a control, we first assessed the localization of the GPI-anchored mCherry reporter protein in GPAA1 KO cells. As anticipated, the mCherry signal was primarily observed at the cell surface in parental OVCAR8 cells, but in GPAA1 KO cells, the mCherry signal was not detectable on the cell surface and was instead predominantly localized within the ER (Figure 4C). Moreover, the complete absence of cell-surface expression of the SBP-mCherry-GPI reporter in GPAA1 KO cells was also confirmed by flow cytometry (Figure 4D). Subsequently, we examined the impact of bestatin treatment on mCherry-GPI cell-surface expression, revealing a notable reduction in cell-surface presentation, as evidenced by confocal microscopy (Figure 4E) and flow cytometry (Figure 4F). These results suggest that bestatin inhibits GPAA1 function, impairing GPI anchoring.

Next, we evaluated the impact of bestatin on cell-surface expression of CD24 in ovarian cancer cell lines. As expected, bestatin treatment led to decreased CD24 cell-surface expression in OVCAR8 (Figure 4G) and SKOV3 (Figure 4H) cells and also reduced cell-surface expression of other GPI-APs tested (Figure S7A). Notably, bestatin treatment did not affect cell proliferation of ovarian cancer cells (Figure S7B). Importantly, bestatin had no significant effect on total CD24 levels, as assessed by flow cytometry following cell permeabilization (Figure S7C), indicating that bestatin specifically decreases cell-surface expression of CD24 without affecting intracellular CD24 levels. Finally, shRNA-mediated knockdown of either CD13 or LTA4H, two well-known targets of bestatin,[51,52] had no effect on CD24 cell-surface expression (Figures S7D–S7G), strongly suggesting that the ability of bestatin to reduce CD24 cell-surface expression is due to its inhibition of GPAA1.

## Bestatin, alone or in combination with docetaxel, inhibits growth of human ovarian cancer xenografts in mice

Because bestatin treatment reduced CD24 cell-surface expression, we hypothesized that bestatin could, like GPAA1 depletion, augment phagocytosis of ovarian cancer cells and inhibit tumor growth. In an *in vitro* phagocytosis assay, we found that bestatin treatment increased macrophage-mediated phagocytosis of OVCAR8, SKOV3, and OVCAR3 cells compared with DMSO-treated cells (Figures 5A–5C). As expected, bestatin treatment of A2780 cells, which lack CD24 expression, did not result in a significant increase in phagocytosis compared with DMSO-treated cells (Figure 5D), strongly suggesting the specificity of bestatin in targeting CD24-dependent mechanisms.

To determine the effect of bestatin treatment on *in vivo* phagocytosis and ovarian tumor growth, we intraperitoneally implanted OVCAR8 or SKOV3 cells expressing GFP and luciferase in NSG mice. After 1 week, bestatin or vehicle was administered through intraperitoneal injection. As shown in Figures 5E and 5F, bestatin treatment resulted in a substantial reduction in tumor growth compared with the control vehicle-treated group. A hallmark of ovarian cancer that is also observed in mouse models is the build-up of fluid in the peritoneal cavity,[34] and we found that bestatin-treated mice exhibited significantly reduced ascites accumulation compared with vehicle-treated mice (Figures 5G and 5H). Furthermore, *in vivo* phagocytosis assays showed that bestatin-treated mice exhibited substantially increased $GFP^+$ $F4/80^+$ double-positive cells, indicative of macrophage-mediated engulfment of ovarian cancer cells (Figures 5I and 5J).

Combination therapies are often used to enhance the efficacy of treatment relative to monotherapies by targeting critical

(F) Left: representative *in vivo* bioluminescence images of C57BL/6 mice 4 weeks after implantation with parental or Gpaa1 KO BPPNM cells. Right: quantitation of tumor growth, as measured by total flux. Data are represented as mean ± SEM ($n = 5$ mice per group).
(G) Left: image showing omental tumors derived from implantation of parental or Gpaa1 KO BPPNM cells. Right: quantification of tumor weight. Data are represented as mean ± SD ($n = 5$ mice per group).
(H) Survival analysis of C57BL/6 mice ($n = 6$ mice per group), harboring tumors derived from implantation of parental or Gpaa1 KO BPPNM cells.
(I) Boxplot showing immunophenotypic quantification of $CD45^+$, $CD3^+$, and $CD8^+$ immune cells in peritoneal fluid derived from parental or Gpaa1 KO BPPNM tumors. Data are represented as mean ± SD ($n = 5$ mice per group).
(J) Representative immunohistochemistry images showing $CD8^+$ T cell infiltration in omental tumors derived from implantation of parental or Gpaa1 KO BPPNM cells. Scale bar, 10 μM.
The $p$ values were calculated using one-way ANOVA followed by Dunnett's multiple-comparisons test for (B), two-way ANOVA with multiple comparisons for (C) and (F), a log rank (Mantel-Cox) test (D) and (H), and a two-tailed unpaired Student's t test for (E), (G), and (I). $^*p < 0.05$, $^{**}p < 0.01$, $^{***}p < 0.001$. See also Figure S3.

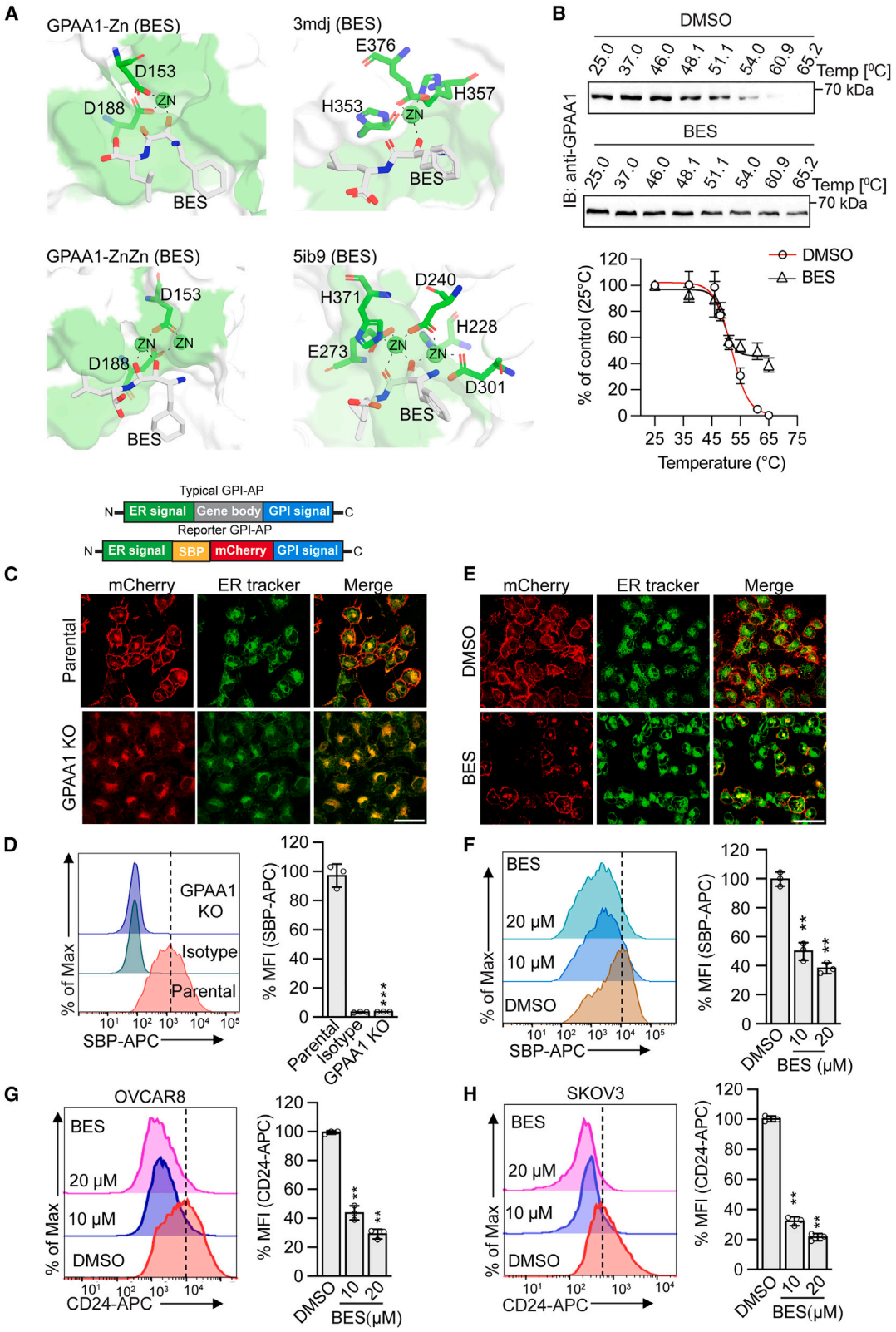


*(legend on next page)*

pathways synergistically or additively. We therefore hypothesized that simultaneous suppression of the CD24 phagocytic checkpoint and induction of a pro-phagocytic signal, such as surface localization of calreticulin (CALR),[53,54] could augment phagocytosis and suppress tumor growth more effectively. To induce CALR, we used docetaxel, a conventional first-line chemotherapeutic drug for ovarian cancer[55,56] that has been shown to induce surface localization of CALR.[57] Consistent with this idea, we found that docetaxel efficiently induced CALR cell-surface expression in OVCAR8 cells, whereas two other chemotherapeutic agents, carboplatin and doxorubicin, did not (Figures 5K and S8). Moreover, combination treatment with bestatin and docetaxel promoted *in vitro* phagocytosis of OVCAR8 cells better than either treatment alone (Figure 5L). Finally, we assessed the impact of combined treatment with bestatin and docetaxel on tumor growth in mice. In this experiment, OVCAR8 cells were subcutaneously implanted into NSG mice, and once tumors were established, the mice were treated with vehicle, bestatin, or docetaxel or a combination of both drugs, and tumor volume was monitored weekly. The results showed that, compared with single-agent treatment, combination treatment significantly reduced tumor growth (Figure 5M). These findings suggest that activating the pro-phagocytic CALR signal may enhance the ability of bestatin to inhibit ovarian tumor growth.

## DISCUSSION

The CD24-Siglec10 axis, initially identified as an inflammatory response regulator in tissue injury,[58] now falls within the category of phagocytic immune checkpoint axes, akin to CD47-SIRP$\alpha$,[59] B2M-LILRB1,[60] and PDL1-PD1.[61] Recent studies have highlighted CD24 as a potential immunotherapeutic target in various cancers.[10,29,62,63] In the ovarian tumor microenvironment, CD24 is predominantly expressed in malignant tumor cells (Figure 2A). In contrast, CD47, another anti-phagocytic signal, is widely expressed across all cell types.[10] Thus, targeting CD24 may offer the advantage of fewer off-target effects, potentially reducing the risk of toxicity.[64]

Preclinical studies targeting the CD24-Siglec10 axis using monoclonal antibodies (mAbs) or bispecific peptides have shown promising results, particularly in boosting phagocytic activity in CD24$^+$ tumors by TAMs.[10,33,65] However, the therapeutic efficacy and safety of these interventions have not been tested in clinical settings. Although humanized mAbs targeting CD24 hold potential as cancer immunotherapeutics,[66] small-molecule therapeutics offer several advantages, including better penetration into solid tumors, reduced immunogenicity, lack of Fc-mediated side effects often observed with mAbs, oral administration convenience, and reduced production costs.[67,68]

In this study, we identified GPAA1 as a factor that plays a crucial role in facilitating cell-surface localization and expression of CD24 and showed that a small-molecule inhibitor of GPAA1, bestatin, reduced ovarian tumor growth by inducing macrophage-mediated phagocytosis. Notably, previous studies have reported that bestatin, or its derivative LYP, may reduce ovarian cancer growth by directly killing cancer cells through inhibition of aminopeptidase N (APN/CD13) activity.[69] However, in our experiments, we did not observe any significant effect of bestatin on cell viability, even at very high concentrations, suggesting that the primary mechanism of bestatin-mediated tumor reduction in ovarian cancer is through an immune-mediated mechanism rather than a direct effect on cell viability. The results of our study highlight the potential of targeting GPAA1 as a therapeutic approach for CD24$^+$ ovarian cancers. In addition, we found that shRNA-mediated knockdown of other factors involved in GPI biosynthesis, such as PIGM, PIGN, PIGO, PIGP, PIGT, and PIGU, which were also identified from our primary screen, also led to a reduction in CD24 cell-surface levels, suggesting the GPI biosynthesis pathway as a broader immunotherapeutic target. Interestingly, although the GPI biosynthesis pathway is crucial for the viability of yeast and protozoans, in mammals it is thought to be non-essential.[70] Consistent with this idea, we observed that the KO of GPAA1 in multiple ovarian cancer cell lines did not result in a proliferation defect. Moreover, knockdown of other components of the GPIT complex, such as PIGM, PIGN, PIGO, PIGP, PIGT, and PIGU, was well tolerated in ovarian

**Figure 4. Bestatin binds to GPAA1 and inhibits GPIT activity**

(A) Molecular modeling of bestatin binding modes in the GPAA1$^{Zn}$ (top left) and GPAA1$^{ZnZn}$ (bottom left) models compared with the reference aminopeptidase-bestatin complexes PDB: 3MDJ (one Zn, top right) and PDB: 5IB9 (two Zn, bottom right). The bestatin molecule is shown as sticks (carbon, white; nitrogen, blue; oxygen, red; others, yellow; hydrogen is not shown for simplicity), the aminopeptidase pockets are shown as surfaces with the Zn in spheres. The pocket residues that are within 4 Å of bestatin (BES) are shown in green. The Zn-interacting residues are labeled.

(B) Cellular thermal stability shift assay. Top: immunoblot analysis monitoring GPAA1 levels at increasing temperatures in the presence of bestatin or vehicle (DMSO). Bottom: the shift in bestatin binding to GPAA1 was analyzed by the Boltzmann sigmoid equation. All data were normalized to the response observed under DMSO treatment conditions at 25°C. Data are represented as mean ± SD ($n$ = 3 independent experiments).

(C) Top: Schematics of a typical GPI-AP and the mCherry-SBP-tagged reporter GPI-AP. Bottom: representative immunofluorescence images showing localization of mCherry in parental or GPAA1 KO OVCAR8 cells expressing the mCherry-SBP-tagged reporter GPI-AP. ER tracker and merged images are shown. Scale bar, 50 μm.

(D) Left: representative flow cytometry histograms of SBP cell-surface expression in parental or GPAA1 KO OVCAR8 cells. Right: Quantification of MFI. Data are represented as mean ± SD ($n$ = 3 independent experiments).

(E) Representative immunofluorescence images showing localization of mCherry in OVCAR8 cells expressing the mCherry-SBP tagged reporter GPI-AP and treated with DMSO or 20 μM bestatin. ER tracker and merge images are shown. Scale bar, 50 μm.

(F) Left: representative flow cytometry histograms of SBP cell surface expression in OVCAR8 cells treated with DMSO or 10 or 20 μM bestatin. Right: quantification of MFI. Data are represented as mean ± SD ($n$ = 3 independent experiments).

(G and H) Left: representative flow cytometry histograms of CD24 cell-surface expression in OVCAR8 (G) or SKOV3 (H) cells treated with DMSO or 10 or 20 μM bestatin. Right: quantification of MFI. Data are represented as mean ± SD ($n$ = 3 independent experiments).

The $p$ values were calculated using a two-tailed unpaired Student's t test for (D) and one-way ANOVA followed by Dunnett's multiple-comparisons test for (F)–(H). $^{**}p < 0.01$, $^{***}p < 0.001$. See also Figures S4–S7.

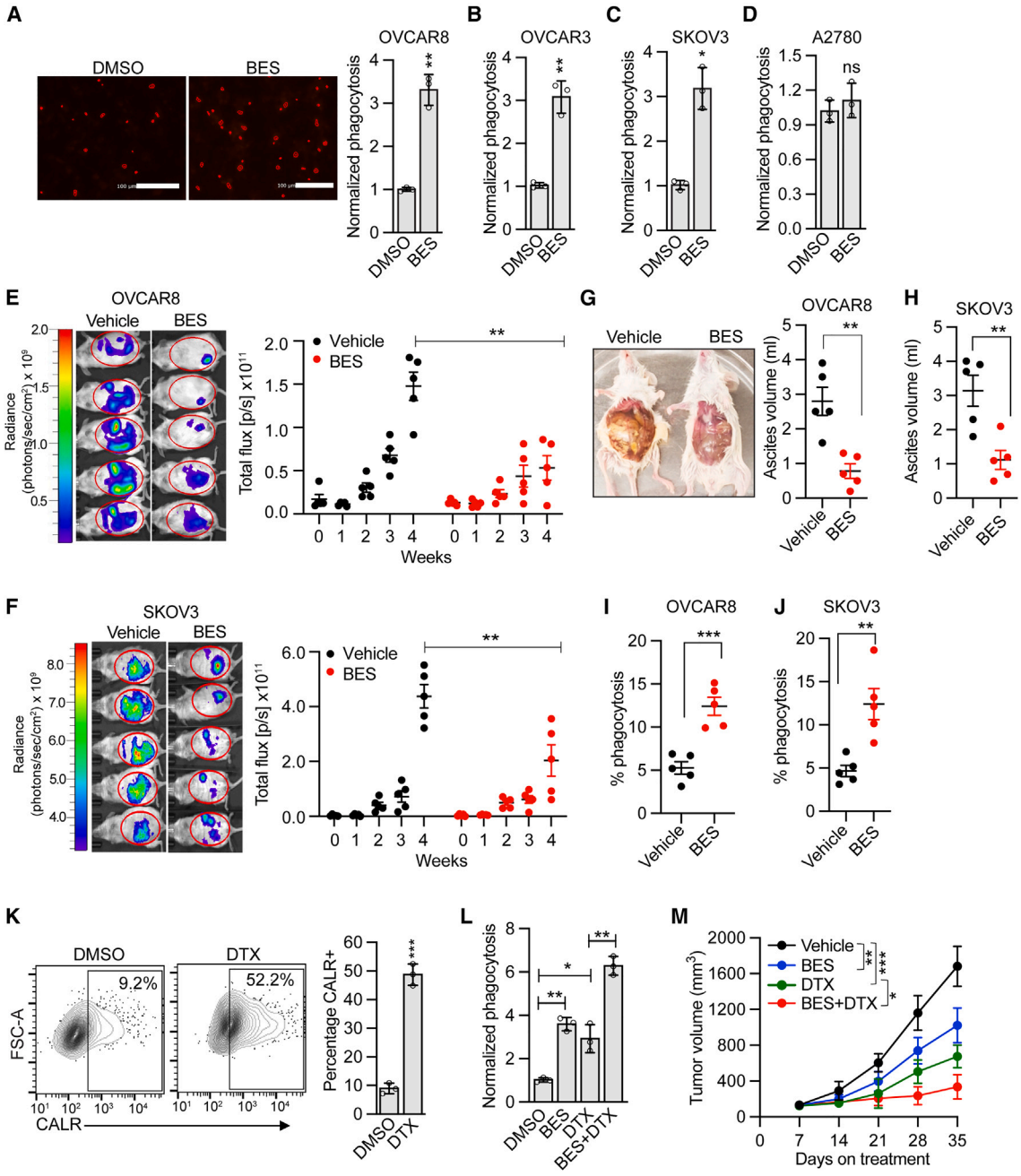


**Figure 5. Bestatin treatment increases phagocytosis and inhibits the growth of human ovarian cancer xenografts in mice**

(A) *In vitro* phagocytosis assay. Representative images (left) and quantification (right) of macrophage-mediated phagocytosis of OVCAR8 cells treated with bestatin (20 μM) or, as a control, DMSO. The results were normalized to that obtained with DMSO. Scale bars, 100 μm. Data are represented as mean ± SD ($n$ = 3 independent experiments).

(B–D) Quantification of macrophage-mediated phagocytosis of OVCAR3 (B), SKOV3 (C), and A2780 (D) cells treated with bestatin (20 μM) or DMSO. The results were normalized to that obtained with DMSO. Data are represented as mean ± SD ($n$ = 3 independent experiments).

(E and F) Left: representative *in vivo* bioluminescence images of NSG mice 5 weeks following implantation with OVCAR8 (E) or SKOV3 (F) cells and treated with bestatin or vehicle. Right: tumor growth, as measured by total flux. Data are represented as mean ± SEM ($n$ = 5 mice per group).

(G) Left: representative image depicting peritoneal ascites accumulation in mice 5 weeks following implantation with OVCAR8 cells and treatment with either vehicle or bestatin. Right: quantification of ascites volume from vehicle or bestatin-treated mice. Data are represented as mean ± SEM ($n$ = 5 mice per group).

(H) Quantification of ascites volume in mice 5 weeks after implantation with SKOV3 cells and treatment with vehicle or bestatin. Data are represented as mean ± SEM ($n$ = 5 mice per group).

*(legend continued on next page)*

cancer cells. Notably, like GPAA1, several other components of the GPI pathway are aberrantly expressed in many cancers, including ovarian cancer.[22] Many of these GPI pathway proteins are enzymatic and therefore of potential therapeutic interest. However, despite attempts to target the GPI pathway in fungal and protozoan pathogens,[70–72] targeted inhibition of the pathway in mammalian systems has proven difficult.[72] To date, targeting of GPI pathway proteins has not yet been explored in the context of cancer.

Prompted by previous studies showing that GPAA1 has a catalytic site that is structurally similar to that of metallo-aminopeptidases[29] and is suggested to function as a metallo-peptide synthetase catalyzing the creation of a peptide bond between the carboxyl group of the substrate protein and the phosphoethanolamine of the mature GPI lipid anchor,[27] we anticipated that the inhibition of this potential enzymatic function could be achieved using commercially available APIs. Our results convincingly show that the implied GPAA1 function can indeed be pharmacologically targeted by several APIs, including bestatin, tosedostat, and ARM-1. Because the three compounds share similar pharmacophores, such as hydrophobic and/or aromatic groups and hydrogen bond acceptors, their interaction mechanism with GPAA1 is most likely similar. Indeed, our computational docking efforts of bestatin and GPAA1 recovered molecular arrangements observed in known 3D structures of aminopeptidase inhibitor complexes, in which a metal ion is encircled by hydrogen acceptor groups of the inhibitor and the compound is embedded in a binding pocket that is collocated with the active site.

Our work provides the first experimental evidence for the theoretically deduced metallo-peptide synthetase activity of GPAA1.[27] Notably, our results are in agreement with previous studies that convincingly associate GPAA1 with the process of GPI lipid anchor attachment (a process that has been shown to be independent and separable of cleavage of the C terminus of the substrate protein by the caspase-like protease PIGK, which generates the substrate for GPI anchor attachment)[13,18,20,73] and with 3D structural data for GPAA1 (except for some details, including the Zn ions near the active site, which might result from issues of sample preparation and structural resolution).[14,19,27,50,73]

At the same time, our experimental findings in this study and previous work[14,27] are in conflict with two published, almost identical cryoelectron microscopy (cryo-EM) structures of the GPIT complex[19,50] that cannot rationalize a catalytic involvement of GPAA1 in the process of GPI lipid anchor attachment. How can this conflict be resolved? First, recent work by Ness et al.[74] reaffirmed that GPAA1 is an essential subunit within the minimal complex with GPI lipid transferase activity. They advanced the idea of dimerization and speculated that the process might involve the spatial vicinity of active sites of PIGK and GPAA1 from different complex entities. Second, it can also not be excluded that previously published cryo-EM structures do not represent catalytically active GPIT conformations as a result of sample preparation or certain assumptions in the structure modeling. Supporting the latter point of view is a recently reported structure of the GPIT complex together with model ligands, which shows PIGK and GPAA1 in cooperating vicinity and with metal ions interacting with the phosphoethanolamine attached to the GPI lipid anchor.[73] A direct enzymatic assay with an *in vitro*-reconstructed GPIT complex will be necessary to evaluate the activity of individual GPIT subunits and the mechanism of action of APIs that disrupt GPIT function.

In summary, the findings of this study highlight the potential for therapeutic targeting of CD24 through GPAA1 inhibition using small-molecule APIs. Our results encourage further exploration of the GPI pathway as a promising target for small molecule-based immunotherapeutic strategies. Although our research primarily focused on ovarian cancer, it is essential to recognize that GPAA1-mediated CD24 regulation is not limited to ovarian cancer. Consequently, targeting GPAA1 and other components of the GPI synthesis pathway could be a feasible strategy for various CD24-positive cancers, including breast, lung, and colorectal cancers.[9]

## Limitations of the study

Our study reveals that inhibition of the GPIT subunit GPAA1 disrupts the cell surface localization and expression of the immune checkpoint CD24. A rescue experiment, aimed at restoring the membrane surface expression of CD24 in a GPI-independent manner, could have provided further insights into the specific role of the GPAA1-CD24 axis in regulating the phagocytosis of cancer cells by macrophages. The lack of *in vitro* assays for directly evaluating the enzymatic activity of GPAA1 restrained us from precisely determining the specific mechanism of action of bestatin and other APIs on GPAA1 inhibition. Furthermore, our results reveal that the CD24-dependent mechanism is predominant; however, we cannot exclude the possibility that there may be contributions from other GPI-linked proteins in tumor growth and/or phagocytosis.

## STAR★METHODS

Detailed methods are provided in the online version of this paper and include the following:

- KEY RESOURCES TABLE
- RESOURCE AVAILABILITY

(I and J) Quantification of TAM-mediated phagocytosis of OVCAR8 (I) or SKOV3 (J) tumor cells in mice treated with vehicle or bestatin. Data are represented as mean ± SEM ($n$ = 5 mice per group).

(K) Left: representative flow cytometry analysis of CALR in OVCAR8 cells treated with docetaxel (DTX; 100 nM) or DMSO. Right: quantification of CALR$^+$ cells. Data are represented as mean ± SD ($n$ = 3 independent experiments).

(L) Quantification of macrophage-mediated phagocytosis of OVCAR8 cells treated with bestatin, DTX, or both. Data are represented as mean ± SD ($n$ = 3 independent experiments).

(M) Measurement of tumor growth in mice subcutaneously implanted with OVCAR8 cells, and treated with bestatin, DTX, or both. Data are represented as mean ± SEM ($n$ = 5 mice per group).

The $p$ values were calculated using a two-tailed unpaired Student's t test for (A)–(D) and (G)–(L) and two-way ANOVA with multiple comparisons for (E), (F), and (M). $^*p < 0.05$, $^{**}p < 0.01$, $^{***}p < 0.001$. See also Figure S8.

## SUPPLEMENTAL INFORMATION

Supplemental information can be found online at https://doi.org/10.1016/j.celrep.2024.114041.

## ACKNOWLEDGMENTS

This work is dedicated to the memory of Michael R. Green, who suddenly passed away while this work was in progress. His guidance and scientific insights were invaluable to this work. We would like to express our gratitude to Arthur Mercurio and Kishore K. Srivastava for critically reading the manuscript. We thank Robert. A. Weinberg for kindly providing the BPPNM cell line, Magnolia L. Pak for suggestions regarding the CRISPR screen, Huseyin Mehmet for advice on this study, and Lynn Chamberlain for technical assistance. We thank the UMass Chan RNAi Core Facility for providing shRNAs, the FACS Core Facility, the Morphology Core Facility, and the Deep Sequencing Core Facility. We acknowledge financial support from the University of Massachusetts Chan Medical School.

## AUTHOR CONTRIBUTIONS

Conceptualization, A.K.M., S.K.M., and M.R.G.; methodology, A.K.M., T.Y., S.B., R.P.T., C.T.-T.S., N.N.H.P., A.A., A.K., S.R.C., T.M.S., K.H., K.S., L.J.Z., S.K.D., P.R.T.; M.A.K., S.K.M, and F.E.; investigation, A.K.M., T.Y., S.B., R.P.T., A.A., A.K., F.E., S.K.M., and M.R.G; formal analysis, A.K.M., C.T.-T.S., N.N.H.P., K.H., L.J.Z., S.K.D., B.E., F.E., and S.K.M.; visualization, A.K.M., S.K.D., and S.K.M.; resources, F.E., S.K.M., and M.R.G.; supervision, F.E., S.K.M., and M.R.G.; project administration, S.K.M.; writing – original draft, A.K.M. and S.K.M.; writing – reviewing & editing, A.K.M., C.T.-T.S., S.K.D., K.S., P.R.T., M.A.K., F.E., S.K.M., and M.R.G.; funding acquisition, M.R.G. All authors read and approved the final manuscript.

## DECLARATION OF INTERESTS

A.K.M., S.K.M., and M.R.G. are listed as inventors on a patent application filed by the University of Massachusetts Chan Medical School on targeting GPI pathway proteins to treat ovarian cancer.

Received: October 26, 2023
Revised: January 25, 2024
Accepted: March 19, 2024
Published: April 3, 2024

## REFERENCES

1. Siegel, R.L., Miller, K.D., Wagle, N.S., and Jemal, A. (2023). Cancer statistics, 2023. CA. Cancer J. Clin. *73*, 17–48. https://doi.org/10.3322/caac.21763.
2. Armstrong, D.K., Alvarez, R.D., Backes, F.J., Bakkum-Gamez, J.N., Barroilhet, L., Behbakht, K., Berchuck, A., Chen, L.M., Chitiyo, V.C., Cristea, M., et al. (2022). NCCN Guidelines® Insights: Ovarian Cancer, Version 3.2022. J. Natl. Compr. Canc. Netw. *20*, 972–980. https://doi.org/10.6004/jnccn.2022.0047.
3. Pokhriyal, R., Hariprasad, R., Kumar, L., and Hariprasad, G. (2019). Chemotherapy Resistance in Advanced Ovarian Cancer Patients. Biomark. Cancer *11*. https://doi.org/10.1177/1179299x19860815.
4. Patch, A.M., Christie, E.L., Etemadmoghadam, D., Garsed, D.W., George, J., Fereday, S., Nones, K., Cowin, P., Alsop, K., Bailey, P.J., et al. (2015). Whole-genome characterization of chemoresistant ovarian cancer. Nature *521*, 489–494. https://doi.org/10.1038/nature14410.
5. Siminiak, N., Czepczyński, R., Zaborowski, M.P., and Iżycki, D. (2022). Immunotherapy in Ovarian Cancer. Preprint at Onco Targets Ther. https://doi.org/10.1007/s00005-022-00655-8.
6. Ledermann, J.A., Colombo, N., Oza, A.M., Fujiwara, K., Birrer, M.J., Randall, L.M., Poddubskaya, E.V., Scambia, G., Shparyk, Y.V., Lim, M.C., et al. (2020). Avelumab in combination with and/or following chemotherapy vs chemotherapy alone in patients with previously untreated epithelial ovarian cancer: Results from the phase 3 javelin ovarian 100 trial. Gynecol. Oncol. *159*, 13–14. https://doi.org/10.1016/j.ygyno.2020.06.025.
7. Liu, Y.L., Selenica, P., Zhou, Q., Iasonos, A., Callahan, M., Feit, N.Z., Boland, J., Vazquez-Garcia, I., Mandelker, D., Zehir, A., et al. (2020). BRCA Mutations, Homologous DNA Repair Deficiency, Tumor Mutational Burden, and Response to Immune Checkpoint Inhibition in Recurrent Ovarian Cancer. JCO Precis. Oncol. *4*. https://doi.org/10.1200/po.20.00069.
8. Vázquez-García, I., Uhlitz, F., Ceglia, N., Lim, J.L.P., Wu, M., Mohibullah, N., Niyazov, J., Ruiz, A.E.B., Boehm, K.M., Bojilova, V., et al. (2022). Ovarian cancer mutational processes drive site-specific immune evasion. Nature *612*, 778–786. https://doi.org/10.1038/s41586-022-05496-1.
9. Panagiotou, E., Syrigos, N.K., Charpidou, A., Kotteas, E., and Vathiotis, I.A. (2022). CD24: A Novel Target for Cancer Immunotherapy. Preprint at J. Pers. Med. https://doi.org/10.3390/jpm12081235.
10. Barkal, A.A., Brewer, R.E., Markovic, M., Kowarsky, M., Barkal, S.A., Zaro, B.W., Krishnan, V., Hatakeyama, J., Dorigo, O., Barkal, L.J., and Weissman, I.L. (2019). CD24 signalling through macrophage Siglec-10 is a target for cancer immunotherapy. Nature *572*, 392–396. https://doi.org/10.1038/s41586-019-1456-0.
11. Nakamura, K., Terai, Y., Tanabe, A., Ono, Y.J., Hayashi, M., Maeda, K., Fujiwara, S., Ashihara, K., Nakamura, M., Tanaka, Y., et al. (2017). CD24 expression is a marker for predicting clinical outcome and regulates the

epithelial-mesenchymal transition in ovarian cancer via both the Akt and ERK pathways. Oncol. Rep. *37*, 3189–3200. https://doi.org/10.3892/or.2017.5583.

12. Salnikov, A.V., Bretz, N.P., Perne, C., Hazin, J., Keller, S., Fogel, M., Herr, I., Schlange, T., Moldenhauer, G., and Altevogt, P. (2013). Antibody targeting of CD24 efficiently retards growth and influences cytokine milieu in experimental carcinomas. Br. J. Cancer *108*, 1449–1459. https://doi.org/10.1038/bjc.2013.102.
13. Kinoshita, T. (2020). Biosynthesis and biology of mammalian GPI-anchored proteins. Preprint at J. Lipid Res. *10*. https://doi.org/10.1098/rsob.190290.
14. Su, C.T.T., Sinha, S., Eisenhaber, B., and Eisenhaber, F. (2020). Structural modelling of the lumenal domain of human GPAA1, the metallo-peptide synthetase subunit of the transamidase complex, reveals zinc-binding mode and two flaps surrounding the active site. Biol. Direct *15*, 14. https://doi.org/10.1186/s13062-020-00266-3.
15. Mitra, A.K., Davis, D.A., Tomar, S., Roy, L., Gurler, H., Xie, J., Lantvit, D.D., Cardenas, H., Fang, F., Liu, Y., et al. (2015). In vivo tumor growth of high-grade serous ovarian cancer cell lines. Gynecol. Oncol. *138*, 372–377. https://doi.org/10.1016/j.ygyno.2015.05.040.
16. Doench, J.G., Fusi, N., Sullender, M., Hegde, M., Vaimberg, E.W., Donovan, K.F., Smith, I., Tothova, Z., Wilen, C., Orchard, R., et al. (2016). Optimized sgRNA design to maximize activity and minimize off-target effects of CRISPR-Cas9. Nat. Biotechnol. *34*, 184–191. https://doi.org/10.1038/nbt.3437.
17. Kinoshita, T., and Fujita, M. (2016). Thematic Review Series: Glycosylphosphatidylinositol (GPI) Anchors: Biochemistry and Cell Biology Biosynthesis of GPI-anchored proteins: special emphasis on GPI lipid remodeling. J. Lipid Res. *57*, 6–24. https://doi.org/10.1194/jlr.r063313.
18. Eisenhaber, B., Maurer-Stroh, S., Novatchkova, M., Schneider, G., and Eisenhaber, F. (2003). Enzymes and auxiliary factors for GPI lipid anchor biosynthesis and post-translational transfer to proteins. Preprint at Bioessays *25*, 367–385. https://doi.org/10.1002/bies.10254.
19. Xu, Y., Jia, G., Li, T., Zhou, Z., Luo, Y., Chao, Y., Bao, J., Su, Z., Qu, Q., and Li, D. (2022). Molecular insights into biogenesis of glycosylphosphatidylinositol anchor proteins. Nat. Commun. *13*, 2617. https://doi.org/10.1038/s41467-022-30250-6.
20. Liu, S.S., Liu, Y.S., Guo, X.Y., Murakami, Y., Yang, G., Gao, X.D., Kinoshita, T., and Fujita, M. (2021). A knockout cell library of GPI biosynthetic genes for functional studies of GPI-anchored proteins. Commun. Biol. *4*, 777. https://doi.org/10.1038/s42003-021-02337-1.
21. Chen, G., Li, S.Y., Cai, H.Y., and Zuo, F.Y. (2014). Enhanced expression and significance of glycosylphosphatidylinositol anchor attachment protein 1 in colorectal cancer. Genet. Mol. Res. *13*, 499–507. https://doi.org/10.4238/2014.January.21.19.
22. Nagpal, J.K., Dasgupta, S., Jadallah, S., Chae, Y.K., Ratovitski, E.A., Toubaji, A., Netto, G.J., Eagle, T., Nissan, A., Sidransky, D., and Trink, B. (2008). Profiling the expression pattern of GPI transamidase complex subunits in human cancer. Mod. Pathol. *21*, 979–991. https://doi.org/10.1038/modpathol.2008.76.
23. Dolezal, S., Hester, S., Kirby, P.S., Nairn, A., Pierce, M., and Abbott, K.L. (2014). Elevated levels of glycosylphosphatidylinositol (GPI) anchored proteins in plasma from human cancers detected by C. septicum alpha toxin. Cancer Biomark. *14*, 55–62. https://doi.org/10.3233/CBM-130377.
24. Wu, G., Guo, Z., Chatterjee, A., Huang, X., Rubin, E., Wu, F., Mambo, E., Chang, X., Osada, M., Sook Kim, M., et al. (2006). Overexpression of glycosylphosphatidylinositol (GPI) transamidase subunits phosphatidylinositol glycan class T and/or GPI anchor attachment 1 induces tumorigenesis and contributes to invasion in human breast cancer. Cancer Res. *66*, 9829–9836. https://doi.org/10.1158/0008-5472.CAN-06-0506.
25. Cerami, E., Gao, J., Dogrusoz, U., Gross, B.E., Sumer, S.O., Aksoy, B.A., Jacobsen, A., Byrne, C.J., Heuer, M.L., Larsson, E., et al. (2012). The cBio Cancer Genomics Portal: An open platform for exploring multidimensional cancer genomics data. Cancer Discov. *2*, 401–404. https://doi.org/10.1158/2159-8290.CD-12-0095.
26. Lisowska, K.M., Olbryt, M., Dudaladava, V., Pamuła-Piłat, J., Kujawa, K., Grzybowska, E., Jarząb, M., Student, S., Rzepecka, I.K., Jarząb, B., and Kupryjańczyk, J. (2014). Gene expression analysis in ovarian cancer - faults and hints from DNA microarray study. Front. Oncol. *4*, 6. https://doi.org/10.3389/fonc.2014.00006.
27. Eisenhaber, B., Eisenhaber, S., Kwang, T.Y., Grüber, G., and Eisenhaber, F. (2014). Transamidase subunit GAA1/GPAA1 is a M28 family metallo-peptide-synthetase that catalyzes the peptide bond formation between the substrate protein's omega-site and the GPI lipid anchor's phosphoethanolamine. Cell Cycle *13*, 1912–1917. https://doi.org/10.4161/cc.28761.
28. Hitzerd, S.M., Verbrugge, S.E., Ossenkoppele, G., Jansen, G., and Peters, G.J. (2014). Positioning of aminopeptidase inhibitors in next generation cancer therapy. Preprint at Amino Acids *46*, 793–808. https://doi.org/10.1007/s00726-013-1648-0.
29. Aroldi, A., Mauri, M., Parma, M., Terruzzi, E., Fedele, M., Perfetti, P., Cocito, F., Mologni, L., Chiarle, R., Piazza, R., and Gambacorti-Passerini, C. (2021). CD24/Siglec-10 "Don't Eat Me" Signal Blockade Is a Potential Immunotherapeutic Target in Mantle-Cell Lymphoma. Blood *138*, 2276. https://doi.org/10.1182/blood-2021-154086.
30. Yin, S.S., and Gao, F.H. (2020). Molecular mechanism of Tumor Cell Immune Escape Mediated by CD24/Siglec-10. Preprint at. https://doi.org/10.3389/fimmu.2020.01324.
31. Lindner, B., Burkard, T., and Schuler, M. (2020). Phagocytosis assays with different pH-sensitive fluorescent particles and various readouts. Biotechniques *68*, 245–250. https://doi.org/10.2144/BTN-2020-0003.
32. Xu, C., Wu, H., Liu, Y., Li, F., Manne, R.K., and Lin, H.K. (2023). Protocol for detecting macrophage-mediated cancer cell phagocytosis in vitro and in vivo. STAR Protoc. *4*, 101940. https://doi.org/10.1016/j.xpro.2022.101940.
33. Shen, W., Shi, P., Dong, Q., Zhou, X., Chen, C., Sui, X., Tian, W., Zhu, X., Wang, X., Jin, S., et al. (2023). Discovery of a novel dual-targeting D-peptide to block CD24/Siglec-10 and PD-1/PD-L1 interaction and synergize with radiotherapy for cancer immunotherapy. J. Immunother. Cancer *11*, e007068. https://doi.org/10.1136/jitc-2023-007068.
34. Iyer, S., Zhang, S., Yucel, S., Horn, H., Smith, S.G., Reinhardt, F., Hoefsmit, E., Assatova, B., Casado, J., Meinsohn, M.C., et al. (2021). Genetically DEFI ned syngeneic mouse models of ovarian cancer as tools for the discovery of combination immunotherapy. Cancer Discov. *11*, 384–407. https://doi.org/10.1158/2159-8290.CD-20-0818.
35. Tseng, D., Volkmer, J.P., Willingham, S.B., Contreras-Trujillo, H., Fathman, J.W., Fernhoff, N.B., Seita, J., Inlay, M.A., Weiskopf, K., Miyanishi, M., and Weissman, I.L. (2013). Anti-CD47 antibody-mediated phagocytosis of cancer by macrophages primes an effective antitumor T-cell response. Proc. Natl. Acad. Sci. USA *110*, 11103–11108. https://doi.org/10.1073/pnas.1305569110.
36. Li, T., Fu, J., Zeng, Z., Cohen, D., Li, J., Chen, Q., Li, B., and Liu, X.S. (2020). TIMER2.0 for analysis of tumor-infiltrating immune cells. Nucleic Acids Res. *48*, W509–W514. https://doi.org/10.1093/NAR/GKAA407.
37. Grujić, M., and Renko, M. (2002). Aminopeptidase inhibitors bestatin and actinonin inhibit cell proliferation of myeloma cells predominantly by intracellular interactions. Cancer Lett. *182*, 113–119. https://doi.org/10.1016/S0304-3835(02)00086-1.
38. Rich, D.H., Moon, B.J., and Harbeson, S. (1984). Inhibition of Aminopeptidases by Amastatin and Bestatin Derivatives. Effect of Inhibitor Structure on Slow-Binding Processes1,2. J. Med. Chem. *27*, 417–422. https://doi.org/10.1021/jm00370a001.
39. Numao, S., Hasler, F., Laguerre, C., Srinivas, H., Wack, N., Jäger, P., Schmid, A., Osmont, A., Röthlisberger, P., Houguenade, J., et al. (2017). Feasibility and physiological relevance of designing highly potent aminopeptidase-sparing leukotriene A4 hydrolase inhibitors. Sci. Rep. *7*, 13591. https://doi.org/10.1038/s41598-017-13490-1.

40. Mathé, G. (1991). Bestatin, an aminopeptidase inhibitor with a multi-pharmacological function. Preprint at Biomed Pharmacother *45*, 49–54. https://doi.org/10.1016/0753-3322(91)90122-A.

41. Sandanayaka, V., Mamat, B., Mishra, R.K., Winger, J., Krohn, M., Zhou, L.M., Keyvan, M., Enache, L., Sullins, D., Onua, E., et al. (2010). Discovery of 4-[(2S)-2-{[4-(4-Chlorophenoxy)phenoxy]methyl}-1-pyrrolidinyl] butanoic acid (DG-051) as a novel leukotriene A4 hydrolase inhibitor of leukotriene B4 biosynthesis. J. Med. Chem. *53*, 573–585. https://doi.org/10.1021/jm900838g.

42. Alomar, S.A., Alghabban, S.A., Alharbi, H.A., Almoqati, M.F., Alduraibi, Y., and Abu-Zaid, A. (2021). Firibastat, the first-in-class brain aminopeptidase a inhibitor, in the management of hypertension: a review of clinical trials. Avicenna J. Med. *11*, 1–7. https://doi.org/10.4103/ajm.ajm_117_20.

43. Albiston, A.L., Diwakarla, S., Fernando, R.N., Mountford, S.J., Yeatman, H.R., Morgan, B., Pham, V., Holien, J.K., Parker, M.W., Thompson, P.E., and Chai, S.Y. (2011). Identification and development of specific inhibitors for insulin-regulated aminopeptidase as a new class of cognitive enhancers. Preprint at Br J. Pharmacol. *164*, 37–47. https://doi.org/10.1111/j.1476-5381.2011.01402.x.

44. Askonas, L.J., Kachur, J.F., Villani-Price, D., Liang, C.D.D., Russell, M.A., and Smith, W.G. (2002). Pharmacological characterization of SC-57461A (3-[methyl[3-[4-(phenylmethyl)phenoxy]propyl]amino]propanoic acid HCl), a potent and selective inhibitor of leukotriene A4 hydrolase I: In vitro studies. J. Pharmacol. Exp. Ther. *300*, 577–582. https://doi.org/10.1124/jpet.300.2.577.

45. Krige, D., Needham, L.A., Bawden, L.J., Flores, N., Farmer, H., Miles, L.E.C., Stone, E., Callaghan, J., Chandler, S., Clark, V.L., et al. (2008). CHR-2797: An antiproliferative aminopeptidase inhibitor that leads to amino acid deprivation in human leukemic cells. Cancer Res. *68*, 6669–6679. https://doi.org/10.1158/0008-5472.CAN-07-6627.

46. Bodineau, L., Frugière, A., Marc, Y., Inguimbert, N., Fassot, C., Balavoine, F., Roques, B., and Llorens-Cortes, C. (2008). Orally active aminopeptidase A inhibitors reduce blood pressure: A new strategy for treating hypertension. Hypertension *51*, 1318–1325. https://doi.org/10.1161/HYPERTENSIONAHA.107.098772.

47. Ota, K., and Uzuka, Y. (1992). Clinical trials of bestatin for leukemia and solid tumors. Biotherapy *4*, 205–214. https://doi.org/10.1007/BF02174207.

48. Trott, O., and Olson, A.J. (2010). AutoDock Vina: Improving the speed and accuracy of docking with a new scoring function, efficient optimization, and multithreading. J. Comput. Chem. *31*, 455–461. https://doi.org/10.1002/jcc.21334.

49. Jafari, R., Almqvist, H., Axelsson, H., Ignatushchenko, M., Lundbäck, T., Nordlund, P., and Martinez Molina, D. (2014). The cellular thermal shift assay for evaluating drug target interactions in cells. Nat. Protoc. *9*, 2100–2122. https://doi.org/10.1038/nprot.2014.138.

50. Zhang, H., Su, J., Li, B., Gao, Y., Liu, M., He, L., Xu, H., Dong, Y., Zhang, X.C., and Zhao, Y. (2022). Structure of human glycosylphosphatidylinositol transamidase. Nat. Struct. Mol. Biol. *29*, 203–209. https://doi.org/10.1038/s41594-022-00726-6.

51. Yamashita, M., Wada, H., Eguchi, H., Ogawa, H., Yamada, D., Noda, T., Asaoka, T., Kawamoto, K., Gotoh, K., Umeshita, K., et al. (2016). A CD13 inhibitor, ubenimex, synergistically enhances the effects of anticancer drugs in hepatocellular carcinoma. Int. J. Oncol. *49*, 89–98. https://doi.org/10.3892/ijo.2016.3496.

52. Zhao, S., Yao, K., Li, D., Liu, K., Jin, G., Yan, M., Wu, Q., Chen, H., Shin, S.H., Bai, R., et al. (2019). Inhibition of LTA4H by bestatin in human and mouse colorectal cancer. EBioMedicine *44*, 361–374. https://doi.org/10.1016/j.ebiom.2019.05.008.

53. Feng, M., Chen, J.Y., Weissman-Tsukamoto, R., Volkmer, J.P., Ho, P.Y., McKenna, K.M., Cheshier, S., Zhang, M., Guo, N., Gip, P., et al. (2015). Macrophages eat cancer cells using their own calreticulin as a guide: Roles of TLR and Btk. Proc. Natl. Acad. Sci. USA *112*, 2145–2150. https://doi.org/10.1073/pnas.1424907112.

54. Sheng, D., Ma, W., Zhang, R., Zhou, L., Deng, Q., Tu, J., Chen, W., Zhang, F., Gao, N., Dong, M., et al. (2022). Ccl3 enhances docetaxel chemosensitivity in breast cancer by triggering proinflammatory macrophage polarization. J. Immunother. Cancer *10*, e003793. https://doi.org/10.1136/jitc-2021-003793.

55. Vasey, P.A., Atkinson, R., Coleman, R., Crawford, M., Cruickshank, M., Eggleton, P., Fleming, D., Graham, J., Parkin, D., Paul, J., et al. (2001). Docetaxel-carboplatin as first line chemotherapy for epithelial ovarian cancer. Br. J. Cancer *84*, 170–178. https://doi.org/10.1054/bjoc.2000.1572.

56. Vasey, P.A. (2003). Role of docetaxel in the treatment of newly diagnosed advanced ovarian cancer. J. Clin. Oncol. *21*, 136s–144s. https://doi.org/10.1200/jco.2003.02.051.

57. Hodge, J.W., Garnett, C.T., Farsaci, B., Palena, C., Tsang, K.Y., Ferrone, S., and Gameiro, S.R. (2013). Chemotherapy-induced immunogenic modulation of tumor cells enhances killing by cytotoxic T lymphocytes and is distinct from immunogenic cell death. Int. J. Cancer *133*, 624–636. https://doi.org/10.1002/ijc.28070.

58. Chen, G.Y., Tang, J., Zheng, P., and Liu, Y. (2009). CD24 and siglec-10 selectively repress tissue damage - Induced immune responses. Science *323*, 1722–1725. https://doi.org/10.1126/science.1168988.

59. Jiang, Z., Sun, H., Yu, J., Tian, W., and Song, Y. (2021). Targeting CD47 for Cancer Immunotherapy. Preprint at J Hematol. Oncol. https://doi.org/10.1186/s13045-021-01197-w.

60. Barkal, A.A., Weiskopf, K., Kao, K.S., Gordon, S.R., Rosental, B., Yiu, Y.Y., George, B.M., Markovic, M., Ring, N.G., Tsai, J.M., et al. (2018). Engagement of MHC class i by the inhibitory receptor LILRB1 suppresses macrophages and is a target of cancer immunotherapy article. Nat. Immunol. *19*, 76–84. https://doi.org/10.1038/s41590-017-0004-z.

61. Gordon, S.R., Maute, R.L., Dulken, B.W., Hutter, G., George, B.M., McCracken, M.N., Gupta, R., Tsai, J.M., Sinha, R., Corey, D., et al. (2017). PD-1 expression by tumour-associated macrophages inhibits phagocytosis and tumour immunity. Preprint at Nature *545*, 495–499. https://doi.org/10.1038/nature22396.

62. Mishra, A.K., Banday, S., Bharadwaj, R., Ali, A., Rashid, R., Kulshreshtha, A., and Malonia, S.K. (2022). Macrophages as a Potential Immunotherapeutic Target in Solid Cancers. Preprint at Vaccines *11*, 55. https://doi.org/10.3390/vaccines11010055.

63. Zhao, M., Li, J., Chen, F., Han, Y., Chen, D., and Hu, H. (2023). Engineering nanoparticles boost TNBC therapy by CD24 blockade and mitochondrial dynamics regulation. J. Control. Release *355*, 211–227. https://doi.org/10.1016/j.jconrel.2023.01.075.

64. Yang, H., Xun, Y., and You, H. (2023). The landscape overview of CD47-based immunotherapy for hematological malignancies. Preprint at Biomark Res. https://doi.org/10.1186/s40364-023-00456-x.

65. Freile, J.Á., Avtenyuk, N.U., Corrales, M.G., Lourens, H.J., Huls, G., van Meerten, T., Cendrowicz, E., and Bremer, E. (2022). CD24 Is a Potential Immunotherapeutic Target for Mantle Cell Lymphoma. Biomedicines *10*. https://doi.org/10.3390/biomedicines10051175.

66. Shapira, S., Kazanov, D., Padler Karavani, V., Benhar, I., and Arber, N. (2016). Abstract 3805: A novel anti-CD24 monoclonal antibody, humanized and affinity maturated for targeting gastrointestinal cancers. Cancer Res. *76*, 3805. https://doi.org/10.1158/1538-7445.am2016-3805.

67. Imai, K., and Takaoka, A. (2006). Comparing antibody and small-molecule therapies for cancer. Preprint at Nat. Rev. Cancer *6*, 714–727. https://doi.org/10.1038/nrc1913.

68. Gharwan, H., and Groninger, H. (2016). Kinase inhibitors and monoclonal antibodies in oncology: Clinical implications. Preprint at Nat. Rev. Clin. Oncol. *13*, 209–227. https://doi.org/10.1038/nrclinonc.2015.213.

69. Gao, J.J., Gao, Z.H., Zhao, C.R., Yuan, Y., Cui, S.X., Zhang, X.F., Cheng, Y.N., Xu, W.F., Tang, W., and Qu, X.J. (2011). LYP, a novel bestatin derivative, inhibits cell growth and suppresses APN/CD13 activity in human ovarian carcinoma cells more potently than bestatin. Invest. New Drugs *29*, 574–582. https://doi.org/10.1007/s10637-010-9391-9.

70. Yadav, U., and Khan, M.A. (2018). Targeting the GPI biosynthetic pathway. Preprint at Pathog Glob Health *112*, 115–122. https://doi.org/10.1080/20477724.2018.1442764.

71. Tsukahara, K., Hata, K., Nakamoto, K., Sagane, K., Watanabe, N.A., Kuromitsu, J., Kai, J., Tsuchiya, M., Ohba, F., Jigami, Y., et al. (2003). Medicinal genetics approach towards identifying the molecular target of a novel inhibitor of fungal cell wall assembly. Mol. Microbiol. *48*, 1029–1042. https://doi.org/10.1046/j.1365-2958.2003.03481.x.

72. Urbaniak, M.D., Capes, A.S., Crossman, A., O'Neill, S., Thompson, S., Gilbert, I.H., and Ferguson, M.A.J. (2014). Fragment screening reveals salicylic hydroxamic acid as an inhibitor of Trypanosoma brucei GPI GlcNAc-PI de-N-acetylase. Carbohydr. Res. *387*, 54–58. https://doi.org/10.1016/j.carres.2013.12.016.

73. Xu, Y., Li, T., Zhou, Z., Hong, J., Chao, Y., Zhu, Z., Zhang, Y., Qu, Q., and Li, D. (2023). Structures of liganded glycosylphosphatidylinositol transamidase illuminate GPI-AP biogenesis. Nat. Commun. *14*, 5520. https://doi.org/10.1038/s41467-023-41281-y.

74. Ness, T.J., Gamage, D.G., Ekanayaka, S.A., and Hendrickson, T.L. (2022). A Soluble, Minimalistic Glycosylphosphatidylinositol Transamidase (GPI-T) Retains Transamidation Activity. Biochemistry *61*, 1273–1285. https://doi.org/10.1021/acs.biochem.2c00196.

75. Zhang, K., Erkan, E.P., Jamalzadeh, S., Dai, J., Andersson, N., Kaipio, K., Lamminen, T., Mansuri, N., Huhtinen, K., Carpén, O., et al. (2022). Longitudinal single-cell RNA-seq analysis reveals stress-promoted chemoresistance in metastatic ovarian cancer. Sci. Adv. *8*, eabm1831. https://doi.org/10.1126/sciadv.abm1831.

76. Sanjana, N.E., Shalem, O., and Zhang, F. (2014). Improved vectors and genome-wide libraries for CRISPR screening. Preprint at HHS author manuscript *11*, 783–784. https://doi.org/10.1038/nmeth.

77. Doench, J.G., Hartenian, E., Graham, D.B., Tothova, Z., Hegde, M., Smith, I., Sullender, M., Ebert, B.L., Xavier, R.J., and Root, D.E. (2014). Rational design of highly active sgRNAs for CRISPR-Cas9-mediated gene inactivation. Nat. Biotechnol. *32*, 1262–1267. https://doi.org/10.1038/nbt.3026.

78. Boncompain, G., Divoux, S., Gareil, N., De Forges, H., Lescure, A., Latreche, L., Mercanti, V., Jollivet, F., Raposo, G., and Perez, F. (2012). Synchronization of secretory protein traffic in populations of cells. Nat. Methods *9*, 493–498. https://doi.org/10.1038/nmeth.1928.

79. Langmead, B., Trapnell, C., Pop, M., and Salzberg, S.L. (2009). Ultrafast and memory-efficient alignment of short DNA sequences to the human genome. Genome Biol. *10*, R25. https://doi.org/10.1186/gb-2009-10-3-r25.

80. Le, T., Phan, T., Pham, M., Tran, D., Lam, L., Nguyen, T., Truong, T., Vuong, H., Luu, T., Phung, N., et al. (2020). BBrowser: Making Single-Cell Data Easily Accessible. Preprint at bioRxiv. https://doi.org/10.1101/2020.12.11.414136.

81. Friesner, R.A., Murphy, R.B., Repasky, M.P., Frye, L.L., Greenwood, J.R., Halgren, T.A., Sanschagrin, P.C., and Mainz, D.T. (2006). Extra precision glide: Docking and scoring incorporating a model of hydrophobic enclosure for protein-ligand complexes. J. Med. Chem. *49*, 6177–6196. https://doi.org/10.1021/jm051256o.

82. Vangone, A., Schaarschmidt, J., Koukos, P., Geng, C., Citro, N., Trellet, M.E., Xue, L.C., and Bonvin, A.M.J.J. (2019). Large-scale prediction of binding affinity in protein-small ligand complexes: The PRODIGY-LIG web server. Bioinformatics *35*, 1585–1587. https://doi.org/10.1093/bioinformatics/bty816.

83. Zhu, L.J., Gazin, C., Lawson, N.D., Pagès, H., Lin, S.M., Lapointe, D.S., and Green, M.R. (2010). ChIPpeakAnno: A Bioconductor package to annotate ChIP-seq and ChIP-chip data. BMC Bioinf. *11*, 237. https://doi.org/10.1186/1471-2105-11-237.

84. Evers, B., Jastrzebski, K., Heijmans, J.P.M., Grernrum, W., Beijersbergen, R.L., and Bernards, R. (2016). CRISPR knockout screening outperforms shRNA and CRISPRi in identifying essential genes. Nat. Biotechnol. *34*, 631–633. https://doi.org/10.1038/nbt.3536.

85. Schmidtke, P., Le Guilloux, V., Maupetit, J., and Tufféry, P. (2010). fpocket: Online tools for protein ensemble pocket detection and tracking. Nucleic Acids Res. *38*, W582–W589. https://doi.org/10.1093/nar/gkq383.

86. Schneidman-Duhovny, D., Dror, O., Inbar, Y., Nussinov, R., and Wolfson, H.J. (2008). PharmaGist: a webserver for ligand-based pharmacophore detection. Nucleic Acids Res. *36*, W223–W228. https://doi.org/10.1093/nar/gkn187.

87. Pedregosa, F., Varoquaux, G., Gramfort, A., Michel, V., Thirion, B., Grisel, O., Blondel, M., Prettenhofer, P., Weiss, R., Dubourg, V., et al. (2011). Scikit-learn: Machine learning in Python. J. Mach. Learn. Res. *12*.

88. Koes, D.R., and Camacho, C.J. (2012). ZINCPharmer: Pharmacophore search of the ZINC database. Nucleic Acids Res. *40*, W409–W414. https://doi.org/10.1093/nar/gks378.

89. Castle, A.M.R., Salian, S., Bassan, H., Sofrin-Drucker, E., Cusmai, R., Herman, K.C., Heron, D., Keren, B., Johnstone, D.L., Mears, W., et al. (2021). Expanding the Phenotypic Spectrum of GPI Anchoring Deficiency Due to Biallelic Variants in GPAA1. Neurol. Genet. *7*, e631. https://doi.org/10.1212/NXG.0000000000000631.

90. Li, Y., Yang, L., Yang, J., Shi, J., Chai, P., Ge, S., Wang, Y., Fan, X., and Jia, R. (2020). A novel variant in GPAA1, encoding a GPI transamidase complex protein, causes inherited vascular anomalies with various phenotypes. Hum. Genet. *139*, 1499–1511. https://doi.org/10.1007/s00439-020-02192-w.

91. Nguyen, T.T.M., Murakami, Y., Sheridan, E., Ehresmann, S., Rousseau, J., St-Denis, A., Chai, G., Ajeawung, N.F., Fairbrother, L., Reimschisel, T., et al. (2017). Mutations in GPAA1, Encoding a GPI Transamidase Complex Protein, Cause Developmental Delay, Epilepsy, Cerebellar Atrophy, and Osteopenia. Am. J. Hum. Genet. *101*, 856–865. https://doi.org/10.1016/j.ajhg.2017.09.020.

92. Schymkowitz, J., Borg, J., Stricher, F., Nys, R., Rousseau, F., and Serrano, L. (2005). The FoldX web server: An online force field. Nucleic Acids Res. *33*, W382–W388. https://doi.org/10.1093/nar/gki387.

93. Martinez, F.O. (2012). Analysis of gene expression and gene silencing in human macrophages. Curr. Protoc. Immunol. *Chapter 14*, 14.28.1–14.28.23. https://doi.org/10.1002/0471142735.im1428s96.

94. Scott, T.E., Lewis, C.V., Zhu, M., Wang, C., Samuel, C.S., Drummond, G.R., and Kemp-Harper, B.K. (2023). IL-4 and IL-13 induce equivalent expression of traditional M2 markers and modulation of reactive oxygen species in human macrophages. Sci. Rep. *13*, 19589. https://doi.org/10.1038/s41598-023-46237-2.

## STAR★METHODS

### KEY RESOURCES TABLE

| REAGENT or RESOURCE | SOURCE | IDENTIFIER |
|---|---|---|
| Antibodies | | |
| APC anti-human CD24 (ML5) | BioLegend | Cat# 311118<br>RRID: AB_2072735 |
| PE anti-human CD24 (SN3) | eBioscience | Cat# 12-0247-42<br>RRID: AB_1548678 |
| APC anti-mouse CD24 (M1/69) | BioLegend | Cat# 101814<br>RRID: AB_439716 |
| Anti-β-actin | Millipore Sigma | Cat# A2228<br>RRID: AB_476697 |
| Anti-human CD24 (EPR19925) | Abcam | Cat# ab202073<br>RRID: AB_2904220 |
| APC anti-human β2-microglobulin (A17082A) | BioLegend | Cat# 395711<br>RRID: AB_2801060 |
| PE anti-human HLA-A2 (MHC-class I) (BB7.2) | BioLegend | Cat# 343306<br>RRID: AB_1877227 |
| APC-anti human Siglec-10 (5G6) | BioLegend | Cat# 347606<br>RRID: AB_11203899 |
| APC anti-mouse/human CD11b (M1/70) | BioLegend | Cat# 101212<br>RRID: AB_312795 |
| APC anti-mouse F4/80 (BM8) | BioLegend | Cat# 123116<br>RRID: AB_893481 |
| APC anti-mouse CD8a (53-6.7) | BioLegend | Cat# 100712<br>RRID: AB_312751 |
| PerCP- anti-mouse CD45 (30-F11) | BioLegend | Cat#103130<br>RRID: AB_893339 |
| PE anti-human Calreticulin (EPR3924) | Abcam | Cat# ab209577; RRID: AB_2943490 |
| PE anti-FOLR1 (LK26) | BioLegend | Cat# 908304<br>RRID: AB_2629795 |
| APC anti-human CD55 (JS11) | BioLegend | Cat# 311312<br>RRID: AB_2075856 |
| PE anti-human CD87 (VIM5) | BioLegend | Cat# 336906<br>RRID: AB_2165468 |
| APC anti-human CD47 (CC2C6) | BioLegend | Cat# 323124<br>RRID: AB_2716203 |
| PE anti-human β2-microglobulin (A17082E) | BioLegend | Cat# 395804<br>RRID: AB_2783320 |
| Pacific Blue anti-human CD14 (M5E2) | BioLegend | Cat# 325615<br>RRID: AB_830689 |
| APC anti-human IgG Fc (M1310G05) | BioLegend | Cat# 410712<br>RRID: AB_2565790 |
| PE-*anti*-mouse CD3 (17A2) | BioLegend | Cat# 100205<br>RRID: AB_312662 |
| PE anti-mouse CD206 (C068C2) | BioLegend | Cat# 141706<br>RRID: AB_10895754 |
| PE anti-mouse CD80 (16-10A1) | BioLegend | Cat# 104708<br>RRID: AB_313129 |
| PE anti-mouse CD11b(M1/70) | BioLegend | Cat# 101208<br>RRID: AB_312791 |

(*Continued on next page*)

*Continued*

| REAGENT or RESOURCE | SOURCE | IDENTIFIER |
|---|---|---|
| Anti-mouse CD3 (17A2) | eBioscience | Cat# 14-0032-81<br>RRID: AB_467052 |
| Anti-Mouse CD8a (53-6.7) | eBioscience | Cat# 14-0081-82<br>RRID: AB_467087 |
| TruStain FcX (anti-mouse CD16/32) (93) | BioLegend | Cat# 101320<br>RRID: AB_1574975 |
| Anti-GPAA1 (Polyclonal) | Proteintech | Cat# 10104-1-AP; RRID: AB_2263708 |
| Human TruStain FcX™ | BioLegend | Cat# 422302<br>RRID: AB_2818986 |
| Goat anti-rabbit IgG H&L (Alexa Fluor ®594) | Abcam | Cat# ab150080; RRID: AB_2650602 |
| Anti-GPAA1 (Polyclonal) | Invitrogen | Cat# PA5-100548<br>RRID: AB_2850057 |
| Purified anti-CRISPR (Cas9) antibody (6G12-H11) | BioLegend | Cat# 698302<br>RRID: AB_2715782 |
| **Bacterial and virus strains** | | |
| NEB 5-alpha Competent *E. coli* | New England Biolabs | Cat# C2987 |
| Lentivirus particles | Packaged in house | N/A |
| **Biological samples** | | |
| Leukopaks | Rhode Island Blood Center (Providence, RI) | N/A |
| **Chemicals, peptides, and recombinant proteins** | | |
| RPMI 1640 medium | Thermo Scientific | Cat# 61870036 |
| DMEM with high glucose | HyClone | Cat# SH30022.01 |
| OptiMEM medium | Gibco | Cat# 31985062 |
| Fetal bovine serum (FBS) | R&D Systems | Cat# S11550 |
| Sodium pyruvate | Thermo Scientific | Cat# 11360070 |
| Monocyte Attachment Medium (MAM) | Millipore Sigma | Cat# C-28051 |
| IMDM | Gibco | Cat# 12440053 |
| Non-essential amino acids | Gibco | Cat# 11140050 |
| Penicillin, Streptomycin | Gibco | Cat# 15140122 |
| TrypLE™ Express Enzyme | Gibco | Cat# 12604013 |
| Ficoll Paque Plus | Millipore Sigma | Cat# GE17-1440-02 |
| 1X RBC lysis buffer | eBioscience | Cat# 00-4333-57 |
| Recombinant human M-CSF | PeproTech | Cat# AF-300-25 |
| Recombinant human IL-4 | PeproTech | Cat# 200-04 |
| Recombinant human IL-10 | PeproTech | Cat# 200-10 |
| Recombinant mouse IL-13 | PeproTech | Cat# 210-13 |
| Human Siglec-10 Fc | R&D systems | Cat# 2130-SL |
| Bovine Serum Albumin | Millipore Sigma | Cat# A3294 |
| Clodronate liposomes | Liposoma | Cat# CP-030-030 |
| Effectene transfection reagent | Qiagen | Cat# 301425 |
| Polybrene | Millipore Sigma | Cat# TR-1003-G |
| Crystal violet | Millipore Sigma | Cat# V5265 |
| RIPA Lysis Buffer, 10X | Millipore Sigma | Cat# 20-188 |
| Lenti-X Concentrator | Takara | Cat# 631232 |
| ECL Substrate | Bio-Rad | Cat # 1705061 |
| D-luciferin | Promega | Cat#P1042 |
| Alpha SureFire Ultra Lysis Buffer | PerkinElmer | Cat# ASLU-LB |
| BsmBI-v2 | NEB | Cat# R0739S |

(*Continued on next page*)

*Continued*

| REAGENT or RESOURCE | SOURCE | IDENTIFIER |
|---|---|---|
| PMSF | Millipore Sigma | Cat# 329-98-6 |
| EGF | Millipore Sigma | Cat#SRP3027 |
| ITS-G | Thermo Scientific | Cat# 41400045 |
| Halt™ Protease Inhibitor Cocktail (100X) | Thermo Scientific | Cat# 78430 |
| Bestatin (Ubenimex, NK421) | SelleckChem | Cat# S1591 |
| Tosedostat | MedChemExpress | Cat# HY-14807 |
| ARM-1 | MedChemExpress | Cat# HY-W027340 |
| HFI-142 | MedChemExpress | Cat# HY-110259 |
| Actinonin | MedChemExpress | Cat# HY-113952 |
| Amastatin hydrochloride | MedChemExpress | Cat# HY-115194 |
| SC-57461 | MedChemExpress | Cat# HY-103226 |
| DG051 | MedChemExpress | Cat# HY-10825 |
| Acebilustat | MedChemExpress | Cat# HY-17625 |
| Firibastat | MedChemExpress | Cat# HY-109058 |
| Docetaxel | SelleckChem | Cat# S1148 |
| Carboplatin | SelleckChem | Cat# S1215 |
| Doxorubicin | SelleckChem | Cat# E2516 |
| DMSO | Millipore Sigma | Cat# D8418 |
| Blasticidin | Sigma | Cat# 15205 |
| Puromycin | Sigma | Cat# P8833 |
| Sodium azide | Millipore Sigma | Cat# S2002 |
| 7-AAD | BioLegend | Cat# 420404 |
| Trizol Reagent | invitrogen | Cat# 15596026 |
| Paraformaldehyde | Millipore Sigma | Cat# 158127 |
| Tween 80 | Millipore Sigma | Cat# P4780 |
| Triton X-100 | Millipore Sigma | Cat# 9036-19-5 |
| Goat serum | Gibco | Cat# 16210064 |
| ER-Tracker Blue-White DPX | Invitrogen | Cat# E12353 |
| ProLong Glass Antifade Mountant | Invitrogen | Cat# P36980 |
| pHrodo Red, SE | Invitrogen | Cat# P36600 |
| Matrigel | Sigma | Cat# CLS356237 |
| **Critical commercial assays** | | |
| PrestoBlue Cell Viability Reagent | Thermo Scientifc | Cat# A13261 |
| ProtoScript II First Strand cDNA Synthesis Kit | NEB | Cat# E6560 |
| PureYield Plasmid Miniprep System | Promega | Cat# A1222 |
| PureLink HiPure Plasmid Midiprep Kit | Invitrogen | Cat# K210004 |
| RNeasy Mini kit | Qiagen | Cat# 74104 |
| True-Nuclear Transcription Factor Buffer Set | BioLegend | Cat# 424401 |
| Human Tumor Dissociation Kit | Miltenyi Biotec | Cat#130-095-929 |
| Phusion High-Fidelity PCR Kit | Thermo Scientific | Cat# F553L |
| **Deposited data** | | |
| CRISPRscreen | Zenodo | Zenodo: 10.5281/zenodo.10712119 |
| scRNA-seq data from Zhang et al.[75] | GEO | GEO: GSE165897 |
| LOGpc | GEO | GEO: GSE63885 |
| cBioPortal database | Cerami et al.[25], Li et al.[36] | http://www.cbioportal.org/ |
| TIMER 2.0 | Li et al.[36] | http://timer.cistrome.org/ |

(*Continued on next page*)

*Continued*

| REAGENT or RESOURCE | SOURCE | IDENTIFIER |
|---|---|---|
| Experimental models: Cell lines | | |
| A1847 | Kindly provided by Dr. Sharon Cantor UMass Chan Medical School | N/A |
| OVCAR8 | Creative Biolabs | Cat#IOC-ZP305 |
| SKOV3 | ATCC | HTB-77 |
| OVCAR3 | ATCC | HTB-161 |
| OVCAR4 | Sigma-Aldrich | Cat#SCC258 |
| NCI-ADR-RES | Lab Stock | N/A |
| IGROV1 | Sigma-Aldrich | Cat# SCC203 |
| A2780 | Kindly provided by Dr. Sharon Cantor UMass Chan Medical School | N/A |
| HEK-293T | ATCC | CRL-3216 |
| BPPNM | Kindly provided by Dr. R. Weinberg Massachusetts Institute of Technology | N/A |
| Experimental models: Organisms/strains | | |
| NOD-scid IL2R gamma null (NSG) mice | Jackson Laboratory | RRID:IMSR_JAX:005557 |
| C57BL/6 mice | Jackson Laboratory | RRID:IMSR_JAX:000664 |
| Oligonucleotides | | |
| Sequences for qPCR primers, shRNAs and sgRNAs | See Table S3 | N/A |
| Recombinant DNA | | |
| LentiCRISPRv2 | Sanjana et al.[76] | RRID: Addgene_52961 |
| lentiCas9-Blast | Sanjana et al.[76] | RRID: Addgene_52962 |
| pXPR_011 | Doench et al.[77] | RRID: Addgene_59702 |
| pLenti-Emerald-Green-luc | A gift from Jonathan M Hernandez, NCI. | N/A |
| pCDH_SBP-mCherry-GPI | Boncompain et al.[78] | RRID: Addgene_65299 |
| psPAX2 | gift from Didier Trono | RRID: Addgene_12260 |
| pMD2.G | gift from Didier Trono | RRID: Addgene_12259 |
| Human Brunello CRISPR Knockout Pooled Library | Doench et al.[16] | Addgene #73178 |
| Software and algorithms | | |
| Bowtie (version 1.2.2) | Langmead et al.[79] | https://bio.tools/bowtie |
| Illustrator 2022 | Adobe | https://www.adobe.com/products/illustrator.html |
| Bio Turing Inc. | Le et al.[80] | https://bioturing.com/ |
| IVIS Spectrum CT | Perkin-Elmer | https://www.perkinelmer.com/uk/product/ivis-instrument-spectrum-ct-120v-128201 |
| IVIS Living Image 4.0 | Perkin-Elmer | https://www.perkinelmer.com/uk/category/in-vivo-imaging-software |
| FlowJo v10 | FlowJo, LLC | RRID: SCR_008520 |
| ImageJ | https://imagej.nih.gov/ij/download.html | N/A |
| Fiji | https://imagej.net/software/fiji/ | N/A |
| AutoDock Vina | Trott et al.[48] | https://vina.scripps.edu/ |
| Glide v8.8 | Friesner et al.[81] | N/A |
| PRODIGY-LIG | Vangone et al.[82] | https://github.com/haddocking/prodigy-lig |
| Bioconductor package ChIPpeakAnno | Zhu et al.[83] | https://bioconductor.org/packages/release/bioc/html/ChIPpeakAnno.html |
| R package CRISPRscreen | github | https://github.com/LihuaJulieZhu/CRISPRscreen |
| BioRender | BioRender | https://www.biorender.com/ |
| Prism 9.0 | GraphPad | https://www.graphpad.com/ |

## RESOURCE AVAILABILITY

### Lead contact

Further information and requests for resources should be directed to and will be fulfilled by the lead contact, Sunil K. Malonia (sunil.malonia@umassmed.edu).

### Materials availability

This study did not generate new unique reagents.

### Data and code availability

- The data reported in this paper will be shared by the lead contact upon request.
- This paper analyzes existing, publicly available data; the accession numbers for these datasets are listed in the key resources table.
- The original code has been deposited at Zenodo as an R package CRISPRscreen https://zenodo.org/doi/10.5281/zenodo.10712119.
- Any additional information required to reanalyze the data reported in this paper is available from the lead contact upon request.

## EXPERIMENTAL MODEL AND STUDY PARTICIPANT DETAILS

### Cell culture

Human ovarian cancer cell lines A2780, A1847, IGROV1, OVCAR3, OVCAR4, OVCAR8, SKOV3, and NCI/ADR-RES were cultured in RPMI 1640 medium. The HEK293T cell line was maintained in Dulbecco's Modified Eagle Medium (DMEM) with high glucose media supplemented with 10% fetal bovine serum (FBS), sodium pyruvate, non-essential amino acids, 100 units/ml penicillin and 100 μg/mL streptomycin. All cell lines were cultured at 37°C and 5% $CO_2$. Sublines derived from OVCAR3, OVCAR8, and SKOV3 were cultured in the same conditions as the parental cell lines. The BPPNM (*Brca1*$^{-/-}$*Trp53*$^{-/-}$*R172HPten*$^{-/-}$*Nf1*$^{-/-}$*Myc*$^{OE}$) cell line and its sublines were cultured DMEM supplemented with 1% insulin–transferrin–selenium (ITS-G), EGF (2 ng/mL), 4% heat-inactivated fetal bovine serum, 100 units/ml penicillin and 100 μg/mL streptomycin.

### Animal studies

All mouse studies were performed using 6-7-week-old female NOD *scid* gamma (NSG) or C57BL/6 mice in accordance with the Guide for the Care and Use of Laboratory Animals from NIH, and a protocol (202000105) approved by the UMass Chan Medical School Institutional Animal Care and Use Committee (IACUC).

## METHOD DETAILS

### Lentivirus packaging, transduction, and shRNA knockdown

To package lentiviral shRNAs, 1x10$^6$ HEK293T cells were transfected with lentiviral shRNA or transgene vectors and packaging plasmids psPAX2 and pMD2.G mixed in a 2:2:1 ratio. Transfection was performed using an Effectene transfection reagent. The next day, the medium was replaced to remove DNA complexes. After 48 h, post-transfection medium containing lentiviral particles was collected and filtered through a 0.45 μm filter.

For shRNA knockdown, 1x10$^5$ cells per well were seeded in 6-well plates and transduced with lentivirus expressing an shRNA or a non-silencing shRNA (listed in Table S3) in a total volume of 1 mL of appropriate medium supplemented with 10 μg/mL polybrene. The medium was replaced after overnight incubation to remove polybrene and viral particles and cells were selected with puromycin (2 μg/mL) for 4–5 days.

### CRISPR/Cas9 screen

To generate a stable Cas9-expressing OVCAR8 cell line, the plasmid lentiCas9-blast was packaged into a lentivirus as described above, and the viral supernatant was used to transduce the target cells. Cells were selected for 5 days with blasticidin (5 μg/mL) and single-cell clones were isolated and tested for Cas9 gene editing efficiency using the Cas9 reporter vector pXPR_011. For the screen, 8x10$^7$ OVCAR8/Cas9 cells were transduced with the Human Brunello CRISPR Knockout Pooled Library[16] at a multiplicity of infection (MOI) of 0.5. Cells were selected with 2 μg/mL puromycin for 15 days and then stained with an APC-conjugated anti-human CD24 antibody for 30 min on ice in the dark. Five to 10 min prior to FACS, 7-AAD solution was used to exclude dead cells from the analysis. At least 1x10$^8$ CRISPR-edited cells were FACS sorted to isolate the CD24$^{low}$ (defined as cells with the 5% lowest CD24 staining) and 7AAD$^{neg}$ population. Total genomic DNA was extracted from the CD24$^{low}$ and unsorted populations and was used to prepare next-generation sequencing libraries as previously described,[84] which were sequenced using Illumina technology. The quality of the raw reads was assessed using FastQC (version 0.11.5). The 20-bp sequences immediately following the pre-guide RNA sequence "GGCTTTATATATCTTGTGGAAAGGACGAAACACCG" was extracted using a customized Perl script. For mapping the 20 bp reads to the human Brunello library's single guide RNA (sgRNA) sequences, Bowtie (version 1.2.2) was employed with the default

parameters, except for -m 1 –best -v 3[79]. To identify candidate genes for further validation and analysis, Fisher Exact test was performed, and P-values were adjusted using the BH-method to counteract the effects of multiple hypothesis testing. *CRISPRscreen, an* R package, was used for statistical analysis and figure generation *(https://github.com/LihuaJulieZhu/CRISPRscreen)*. Gene Ontology (GO) enrichment analysis was performed using the function getEnrichedGO in Bioconductor package ChIPpeakAnno. GO terms with a P-value <0.001 were considered significant.

### CRISPR knockout generation

For the generation of GPAA1 and CD24 knockout cell lines, sgRNAs targeting the GPAA1 and CD24 genes (listed in Table S3) were cloned into the lenti-CRISPRv2 vector and packaged into lentivirus as described above. Cells were transduced with lentiviral particles and selected in puromycin (2 mg/mL) for 10 days. Single-cell clones were isolated using the serial dilution method in 96-well plates. Individual clones were propagated, and gene-specific knockout was confirmed by immunoblotting using polyclonal antibodies against GPAA1 or CD24.

### Flow cytometry analysis

For cell surface staining, $1x10^5$–$1x10^6$ cells were first incubated with Fc receptor blocking solution for 10 min at room temperature. Cells were washed once in FACS buffer (1X PBS, 1.0% bovine serum albumin (BSA) and 0.2% sodium azide), and then incubated with antibodies for 30 min at 4°C in the dark. Cells were also stained with 7-AAD or DAPI for dead cell exclusion, and flow cytometry analysis was performed using a Bio-Rad ZE5 Cell Analyzer. For intracellular staining, cells were fixed with 1% paraformaldehyde for 5 min and permeabilized using the True-Nuclear Transcription Factor Buffer Set before the addition of the antibody.

### Quantitative RT-PCR

Total RNA was extracted from cells using Trizol. The cDNA was synthesized using Proto Script II reverse transcription kit (NEB) and real-time PCR reactions were performed using a Quant Studio 3 Real-Time PCR system (Applied Biosystems) using primer sequences listed in Table S3. Target gene expression was normalized to that of *GAPDH*.

### Immunoblot analysis

Cells seeded in 6-well plates were harvested and lysed in RIPA buffer (1% Triton X-100, 0.1% SDS, 0.5% deoxycholic acid, 20 mM Tris, pH 7.5, 10% glycerol) containing 1X protease inhibitor cocktail and 1 mM PMSF. Total lysates (30 μg) were run on 10% SDS-PAGE and transferred to nitrocellulose membrane. Membranes were blocked with 5% non-fat dry milk and incubated with the following antibodies overnight at 4°C: anti-GPAA1 (1:1000 dilution), anti-CD24 (1:1,000 dilution), or anti-β-actin (1:2000 dilution). The blots were imaged by exposing them to X-ray film. Experiments were conducted three independent times and the results from one representative experiment are shown.

### Confocal microscopy

To prepare cells for confocal microscopy, cells were grown on coverslips and fixed with 4% paraformaldehyde for 20 min at room temperature followed by three washes with cold 1X PBS. Cells were then permeabilized with 0.3% Triton X-100 for 10 min, washed three times with cold PBS, blocked for 1 h at room temperature with 10% goat serum in PBS, and then incubated at 4°C overnight with recombinant anti-CD24 primary antibody. The cells were then washed three times with PBS, incubated with a fluorescently conjugated secondary antibody (goat anti-rabbit IgG H&L (Alexa Fluor 594) for 1 h at room temperature, and then washed again three times with PBS. For ER staining, cells were incubated with ER-Tracker Blue-White DPX in PBS for 10 min at room temperature. Thereafter, cells were washed three times with PBS before being mounted in ProLong Gold Antifade Mountant. Images were taken using a Leica SP8 Laser Scanning Confocal Fluorescence microscope using a 100× objective lens (oil). The z stack images were taken with a 0.2 mm thick frame. Images were processed and analyzed using Fiji software.

### Small-molecule inhibitor and drug treatments

Ovarian cancer cells were seeded in 96-well plates, and when reached 70% confluency, cells were subjected to treatment with aminopeptidase inhibitors for 48 h with the concentrations as indicated in the figure legends. Dimethyl sulfoxide (DMSO) served as the vehicle control. In the case of chemotherapeutic drugs Docetaxel (100 nM), Carboplatin (100 nM), and Doxorubicin (50 nM), cells were treated for 12 h.

### Analysis of *GPAA1* genomic amplification and Kaplan-Meier analysis

Pan-cancer analysis of genomic amplification of *GPAA1* was performed using the online cBioPortal database (http://www.cbioportal.org). To generate the survival curves for patients expressing high (upper 25%) versus low (other 75%) levels of *GPAA1*, the interactive web server Online consensus Survival analysis for Ovarian cancer (OSov) found at the Long-term Outcome and Gene Expression Profiling Database of pan-cancers (LOGpc) (https://bioinfo.henu.edu.cn/OV/OVList.jsp) was used to query the dataset GEO: GSE63885 (for GPAA1).

### Analysis of scRNA-seq dataset

The Bioturing Talk2data online interactive web tool was used to query the publicly available single-cell RNA (scRNA) dataset (GEO: GSE165897) as previously described.[80] Default parameters were utilized to generate tSNE plots illustrating the expression of CD24 and GPAA1 using BioVinci tool. Cell clusters in the ovarian cancer tumor microenvironment (TME) were identified based on author-defined cell types defined.[75]

### Descriptor extraction of inhibitor-binding pocket features and common pharmacophores of aminopeptidase inhibitors

Inhibitor-bound aminopeptidase complexes were identified from Protein DataBank (PDB, accessed in October 2021) using the "Advanced Search" with the query containing a combination of additional structure keywords: "aminopeptidase" and "inhibitor". Only 107/121 aminopeptidase complexes that contain small molecules as inhibitors were retrieved for analysis; the remaining set of the aminopeptidase inhibitors are peptide-like types and were excluded from further analysis in this computational study (the full list in Table S1). The majority of the structures (82/107) included metals in the inhibitor-binding regions, with 89% (73/82) involving direct metal binding; no information of metals was captured in the other (25/107) complexes. With these variations in mind, we first computed various characteristics of ion and inhibitor binding by aminopeptidases such as numbers of metals in the aminopeptidase active sites and the amino acid residues directly interacting with the ions and the corresponding inhibitors. The *dpocket* module implemented in the *fpocket 2.0* package[85] was used to describe the inhibitor-bound pocket properties such as the amino acid propensity, volume, hydrophobicity and charge scores, as well as the ligand volume. The binding energies were estimated using the PRODIGY-LIG package.[37] PharmaGist server[86] was used to identify pharmacophores, e.g., aromatic, hydrophobic, hydrogen bond donor, and/or acceptor groups, present in the set of 107 aminopeptidase-inhibitor complexes. The resulting features of the inhibitor pharmacophores and the inhibitor-bound pocket amino acid propensities were used to first group the inhibitor set using *k-means* clustering incorporated with principal component (PC) analysis implemented in the scikit-learn v.0.23.2 package.[87] Low variances were observed: ~80% of the total variances explained by the first 6 PCs with the variances maximized within the first 3 PCs. The latter were then used for the *k-means* clustering as labeled in Figure S5A. The same clustering procedure using the first 6 PCs resulted in ~99.1% similar membership (106/107 members remained in the same clusters). Four clusters ($k = 4$) were finalized as the best number of clusters (see clustering evaluation in Figure S5C). Subsequently, the four clusters were further sub-grouped based on the metal binding capacity of the aminopeptidase active sites shown in Figure S5B lacking metal (*no_metal*), with direct metal binding (#*num_metal* > 0), without direct metal binding (#*num_metal* = 0), or different types of metals (ZN, CO, MN, NI, etc.). The common pharmacophores in each sub-cluster of inhibitors were identified using the PharmaGist server with the first molecule in each sub-cluster assigned as the pivot molecule (Figures S5E and S5F). For example, the inhibitor labeled "677" in the aminopeptidase-inhibitor complex PDB: 3hab represents the sub-cluster 0a. Only the alignment against the pivot molecule with the maximum alignment score was selected for each sub-cluster. In cases of a partial alignment (i.e., not all molecules are fully aligned against the pivot molecule), the remaining "not aligned" set of each sub-cluster would undergo the pharmacophore re-search and a new pivot molecule would be re-assigned. If no alignment could be achieved, pharmacophore search for the single molecule would be performed. The common pharmacophores were visualized and analyzed using the ZINC-Pharmer.[88]

### Docking analyses of bestatin to the GPAA1 active sites

Ten replicates were extracted from the molecular dynamics (MD) trajectories of the Zn(s)-bound GPAA1 in our previous study[14] and used to first explore the potential BES-binding pocket on the GPAA1$^{Zn}$ and GPAA1$^{ZnZn}$ structures. Blind docking was first initiated on the 10 replicates (10 × 1000 binding modes) using AutoDock Vina[48] with a grid box centering and covering the whole GPAA1 structure (as receptor). The bestatin molecule retrieved from PubChem (CID: 72172) was used as the ligand. Only those pockets that involved the GPAA1 active sites and the Zn atom(s) and that were most frequently visited by the ligand were of interest. The previous 3 × 300 ns MD samplings of the GPAA1$^{Zn}$ and GPAA1$^{ZnZn}$ models[14] were extended to 3 × 500 ns using the same parameters as previously described. Ten replicates were extracted from the last 300 ns of the new sampling for further docking refinement. In the subsequent focus docking refinement, we used Glide version 8.8 implemented in the Schrödinger package, release 2020-3.[81] The bestatin molecule was prepared and minimized using the LigPrep module. Then, it was docked attentively to the detected region of interest above, i.e., the proximity of the Zn(s)-bound active sites of the GPAA1 structures resulted from the blind docking experiment. For the receptor, a grid box of 7 Å (or 10 Å) was set centering the Zn (or Zns, respectively) coordinated with the GPAA1 active sites that include D153, D188, Y328 and/or E226.[14] The docking protocol with default settings was performed on the extracted 10 replicates of the GPAA1$^{Zn}$ or GPAA1$^{ZnZn}$ conformations. Only those resulting docked complexes with the bestatin binding modes satisfying the detected pharmacophores (i.e., similar to those in the controls PDB: 3mdj and 5ib9) were selected for further analyses. The binding energies were estimated using the PRODIGY-LIG server.[82]

### Computational mutagenesis of the GPAA1 structures

To analyze reported clinical mutations in GPAA1,[89–91] we performed mutagenesis on our GPAA1 models to generate the mutant structures and investigated the protein stability in the presence of the mutations. Among the clinical mutations, six mutations W176S, L290P, L291P,[91] N323S,[90] and H306R, A316V[89] are covered within the length of our lumenal GPAA1 models.[14] They were individually modeled on the GPAA1$^{Zn}$ structure using FoldX 5.0.[92] For each of the mutations, 100 replicates of the mutant

structures were generated for statistical reliability. The respective structural free energy differences between the wildtype and mutants (Δg) were then estimated to investigate the protein structural stability. The alanine scanning was also performed on the GPAA1$^{Zn}$ structure using the *AlaScan* module implemented in the FoldX 5.0 package.

### Cellular thermal shift assay (CETSA)

CETSA assays were performed as described previously.[49] In brief, 1x10$^7$ OVCAR8 cells were treated with DMSO or 100 μM bestatin for 2 h. Cells (50 μL) were aliquoted in PCR tubes and incubated at room temperature (25°C) or at a range of temperatures (37°C–65.2°C) in a thermal cycler for 3 min and cooled to 4°C. Cells were lysed using Alpha SureFire Ultra Lysis Buffer supplemented with Protease Inhibitor Cocktail. Insoluble proteins were separated by centrifugation at 15000xg for 30 min at 4°C. Equal volumes of each sample were separated by SDS-PAGE and detected by immunoblotting blotting using an anti-GPAA1 polyclonal antibody. Three independent experiments were performed. Densitometry of the blots was performed using ImageJ software and the graph was plotted using GraphPad Prism 9.0.

### Macrophage generation and stimulation

Primary human donor-derived macrophages were generated as described previously.[93] In brief, leukopaks from anonymous donors were obtained from the Rhode Island Blood Center (Providence, RI) and peripheral blood monocytes (PBMCs) were isolated by density gradients centrifugation using Ficoll Paque Plus followed by RBC lysis using RBC lysis buffer. For monocyte isolation, PBMCs were incubated in monocyte attachment medium (MAM) for 1 h at 37°C and 5% $CO_2$ and then washed three times in Iscove's Modified Dulbecco's Medium (IMDM) to remove non-adherent cells. The remaining monocytes were detached and seeded in 96-well plates and cultured at 37°C and 5% $CO_2$ in IMDM supplemented with 10% FBS and 20 ng/mL recombinant M-CSF. After 4 days monocytes were then treated with 20 ng/mL recombinant human IL-4 and 10 ng/mL recombinant human IL-13 for another 3-4 days to obtain M2 polarized macrophages.[94] Macrophage differentiation was confirmed morphologically using microscopy. M2-macrophage polarization was confirmed by immunophenotyping of the M2 marker CD206.

### *In vitro* phagocytosis assays

Ovarian cancer cells were labeled with pHrodo Red on ice for 30 min and then co-cultured with PBMC-derived M2 macrophages (prepared as described above) at a ratio of 1:1 (ovarian cancer cells: macrophages) for 4 h in a humidified 5% $CO_2$ incubator at 37°C. Phagocytic events were quantified by counting the number of red fluorescent (pHrodo+) cells per well using a Celigo Imaging Cytometer. GFP was used for the visualization of cancer cells in imaging. Phagocytic events were also quantified using a previously described flow cytometry-based assay.[10,65] In brief, M2-like macrophages co-cultured with EmGFP+ cancer cells in ultra-low attachment 96 plates were harvested and stained with Pacific blue anti-human CD14 and APC anti-human CD11b and analyzed by flow cytometry. The percentage of macrophages undergoing phagocytosis (eaters) was calculated as the percentage of CD11b+ EmGFP+ double-positive cells in the population. For phagocytosis assay with mouse cells (BPPNM), Murine RAW264.7 (RAW) macrophages were cultured in RPMI supplemented with 10% fetal bovine serum and 2% penicillin/streptomycin. For differentiation, cells were stimulated with M-CSF (20 ng/mL) for 48 h, followed by a 72-h stimulation of IL4 (40 ng/mL) and IL13 (40 ng/mL) for M2 polarization.

### Mice experiments

Female NSG mice, 6–7 weeks of age, were injected intraperitoneally with either OVCAR8 (4x10$^6$ cell/mouse) or SKOV3 (5x10$^6$ cells/mouse) EmGFP-luc cells or the corresponding GPAA1 KO EmGFP-luc sublines. Similarly, C57BL/6J mice were implanted with luciferase expressing syngeneic BPPNM cells (4x10$^6$ cells/mouse). Tumors were analyzed using bioluminescence imaging beginning 7 days post-engraftment and continuing every 7 days until day 28. Mice were injected intraperitoneally with luciferin at 140 mg/kg in PBS and images were acquired 10 min later using an IVIS Spectrum CT *In Vivo* Imaging System. Total flux was quantified using Living Image 4.0 software. For survival analysis, deaths were recorded as instances when the tumor burden reached 10 cm of abdominal circumference and/or the body condition scoring values dropped below the threshold specified in our IACUC protocols.

For bestatin treatment, 5x10$^6$ OVCAR8 or SKOV3 cells were implanted in the peritoneal cavity of mice as described above (n = 5 per group), and 7 days later bestatin (100 mg/kg) was administered daily by intraperitoneal injection for 4 weeks. Tumors were analyzed by *in vivo* bioluminescence imaging as described above. For the drug combination experiment, 5x10$^6$ OVCAR8/EmGFP-luc cells were mixed with Matrigel in a 1:1 volume and were implanted subcutaneously in the right flank of NSG mice (n = 5 per group). When tumors reached ~100–150 mm$^3$, mice were treated with either vehicle control (0.9% saline), bestatin (100 mg/kg twice daily by oral gavage), docetaxel (5 mg/kg per week by tail vein injection) or a combination of both bestatin and docetaxel for 28 days. Tumors were measured every week using digital calipers and tumor volumes were calculated using the formula (V = ½ (Length × Width$^2$). Differences between control and treated groups were determined using the two-way ANOVA followed by Turkey's multiple comparison test.

### Macrophage depletion

For macrophage depletion experiments, 200 μL of clodronate liposomes were administered intraperitoneally every 4 days for 16 days before tumor implantation, followed by an injection of 100 μL of clodronate liposomes every 4 days. Depletion of macrophages was verified by flow cytometry analysis of peritoneal fluid using an APC anti-mouse F4/80 antibody.

### *In vivo* phagocytosis assay

An *in vivo* phagocytosis assay was performed as described previously.[10] Briefly, the peritoneal fluid was harvested from mice that were implanted with EmGFP+ ovarian cancer cells as described above. Cells were blocked using TruStain FcX (anti-mouse CD16/32 antibody for 10 min at room temperature and then stained with an APC anti-mouse F4/80 antibody for 30 min on ice in the dark. The percentage of cells undergoing phagocytosis was calculated as the percentage of F4/80+ EmGFP+ double-positive cells in the population.

### Immunophenotyping of tumors

Omental tumors harvested from C57BL/6 mice were minced and dissociated using the Human Tumor Dissociation Kit from Miltenyi Biotec, following the manufacturer's instructions. Single cell suspensions were filtered, and cells were subsequently resuspended in FACS buffer. Cells were stained with anti-mouse; CD45-Pac-Blue, CD3-PE, and CD8-APC antibodies and analyzed by flow cytometry. DAPI was used for viability assessment.

### Immunohistochemistry

Tumor samples were collected from mouse xenografts, preserved in 10% buffered formalin phosphate overnight, and subsequently embedded in paraffin. Blocks were sliced into 5 μm sections slides and stained with an anti-CD8a antibody (at a 1:100 ratio). Morphological examinations were performed at the UMass Chan Medical School Morphology Core Facility.

### Cell viability and proliferation assays

Ovarian cancer cells were transduced with a lentivirus expressing non-silencing (NS) or CD24 shRNA and analyzed for cell proliferation using PrestoBlue Cell Viability Reagent as per the manufacturer's instructions, and relative cell growth was determined. Relative cell viability of OVCAR8 or SKOV3 cells treated with either DMSO or bestatin (10 or 50 mM) was determined using a PrestoBlue assay. For crystal violet staining, OVCAR8, OVCAR3, or SKOV3 cells (1 $X10^4$) were seeded in a 6-well plate and cultured for 5–6 days. Cells were washed with PBS and fixed using 1 mL of 4% paraformaldehyde for 20 min at room temperature. Following two rinses with PBS, the cells were stained with 0.5 mL of 0.1% crystal violet solution (in 10% ethanol) for 20 min. The cells were rinsed twice with PBS, and the plate was scanned.

## QUANTIFICATION AND STATISTICAL ANALYSIS

The statistical tests used to analyze each set of experimental data are indicated in the figure legends. Data were analyzed using a two-tailed unpaired Student's *t*-test to compare between two groups, one-way analysis of variance (ANOVA) for multiple comparisons, and two-way ANOVA for studies with multiple parameters. Data are presented as mean ± SD or ±SEM, and sample numbers (n) are indicated in the figure legends. All statistical analyses were performed using GraphPad Prism 9.0, and $p < 0.05$ was considered statistically significant.